Fall 2020

Analysis of Antenna Designs for the Maximum Power Transmission

Lauryn P. Smith

Recommended Citation

Smith, Lauryn P., "Analysis of Antenna Designs for the Maximum Power Transmission" (2020). *Electronic Theses and Dissertations*. 2181.
https://digitalcommons.georgiasouthern.edu/etd/2181

ANALYSIS OF ANTENNA DESIGNS FOR THE MAXIMUM POWER TRANSMISSION

by

LAURYN SMITH

(Under the Direction of Sungkyun Lim)

ABSTRACT

Since Nikola Tesla discovered wireless power transmission, it has become a very interesting topic of study in the antennas and wireless propagation community. Various aspects and applications for wireless power transmission are studied today, a few of which are investigated in this work. First, various antenna geometries are analyzed for radiative near-field wireless power transfer in terms of electrical field strength. It is determined that the meander antenna is ideal for maximum power transfer in its radiative near-field region, contrary to its far-field behavior. Next, in the application of radio frequency identification, a directive, UHF RFID tag antenna is designed for pavement embedded applications. The antenna covers 72% of the US required bandwidth (902 – 928 MHz) in measurement and has maximum directivity and read range of 7.38 dBi and 14.2ft (4.3 m), respectively. Although the transmitter and receiver antennas' designs are essential parts of the wireless system, power loss to the wireless channel is another critical factor to consider in ensuring the receiver antenna receives the maximum power. Friis transmission equation is studied in detail, and a section of the Georgia Southern University campus is considered for full cellular coverage in the GSM frequency range. Additionally, using the genetic algorithm in parallel, the optimal position for a 60-GHz wireless router is determined to obtain maximum WIFI coverage in a specific house. Finally, the design procedure for a size-reduced, 15-element Yagi antenna is discussed. A comprehensive comparison is conducted demonstrating the importance of the antenna design, with its similar performance to the full-sized Yagi antenna, while its elements are reduced by 45%.

INDEX WORDS: Directive, High gain, Propagation modeling, Radiative near-field wireless power transfer, Radio frequency identification, Wireless power transfer, Wireless power transmission.

ANALYSIS OF ANTENNA DESIGNS FOR THE MAXIMUM POWER TRANSMISSION

by

LAURYN SMITH

B.S., Georgia Southern University, 2018

M. S., Georgia Southern University, 2020

A Thesis Submitted to the Graduate Faculty of Georgia Southern University in Partial

Fulfillment of the Requirements for the Degree

MASTER OF SCIENCE

COLLEGE OF ENGINEERING AND COMPUTING

ANALYSIS OF ANTENNA DESIGNS FOR THE MAXIMUM POWER TRANSMISSION

by

LAURYN SMITH

Major Professor:	Sungkyun Lim
Committee:	Mohammad Ahad Fernando Rios

Electronic Version Approved:
December 2020

DEDICATION

First and foremost, I would like to thank my amazing parents. Without their love, support and sacrifice this would not be possible. I would also like to thank my family and friends for their support and encouragement throughout my program.

ACKNOWLEDGMENTS

I would like to thank my research advisor and mentor, Dr. Sungkyun Lim for giving me the opportunity to obtain this degree and for seeing my potential and always pushing me to reach it. I would also like to thank my committee members, Dr. Rios and Dr. Ahad, for taking the time to review my thesis. Finally, I extend my thanks to Kevin Leon for his help with measurements for publications, so that I could focus on my thesis.

TABLE OF CONTENTS

Page

LIST OF TABLES

Page

LIST OF FIGURES

CHAPTER 1

INTRODUCTION

1.1 Wireless Power Transmission

Wireless Power Transmission (WPT), also known as Wireless Power Transfer, is the transmission of electrical energy without wires or physical connections by utilizing electromagnetic waves. The interest in WPT stems from the ability to increase devices' mobility and eradicate the necessity for cables. WPT has the potential to reduce the environmental impacts associated with supplying power, such as decreasing waste. Since its invention over one hundred years ago, WPT has remained an exciting topic of study. WPT has also become more widely available to charge small electronics like cell phones, watches, and laptops.

1.1.1 History of Wireless Power Transmission

Nikola Tesla, the "Father of Wireless," was the first to demonstrate the possibility of wireless transmission of energy by use of electromagnetic waves in 1891 with his invention, the Tesla coil — and in 1893, he was able to light a bulb using WPT in the World Columbian Exposition in Chicago. He is also known for the Wardenclyffe tower, dubbed the Tesla tower, which he designed and constructed with the goal of implementing WPT worldwide. Although his dream of transmitting power worldwide has yet to be realized, Tesla set the foundation for researchers who have to date been able to design and implement effective WPT systems and advance the technology [1]. In 1964, the first publication regarding WPT was published by Brown, in which a helicopter was entirely powered by electromagnetic waves at 2.4 GHz, a distance of 60 ft above the transmitter antenna [2]. In 1968, the solar-powered satellite came into play [3]. At Goldstone in California and Grand Bassin on Reunion Island in the late 1900s, experiments were conducted with power transferred on the order of 10 kW [4], [5]. In 2007, a group of MIT researchers demonstrated effective WPT of about 40% power transfer efficiency (PTE) at 7ft [6] using two coil antennas. Nissan revealed a prototype inductive leaf for wireless car charging at a Tokyo Auto show in 2012. These are just a few of the advances in WPT since its discovery, and with the interest of researchers and industry professionals in the topic, the technology continues to advance over the years. Since then, various studies have been conducted to design highly efficient wireless power transfer systems and extend the operation range.

1.1.2 Wireless Power Transfer Background

WPT is divided into two main categories, near-field WPT and far-field WPT. Near-field WPT can further be divided into reactive near-field WPT and radiative near-field WPT. The categorization is based on the field regions of an antenna, depicted in Fig. 1.1.

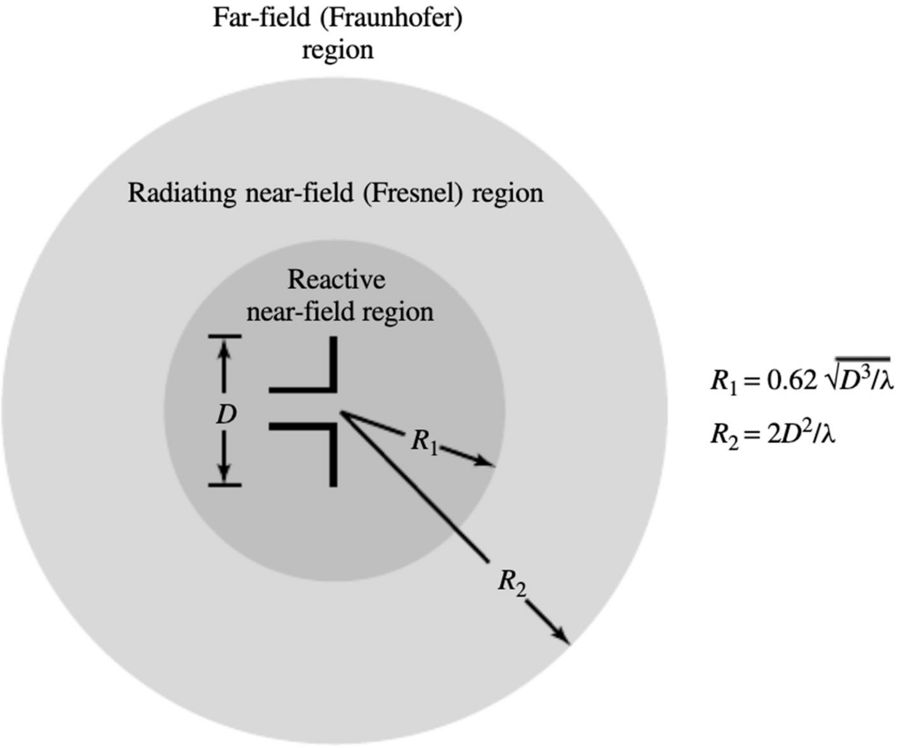

Fig. 1.1. The field regions of an antenna [7].

The reactive near-field region is defined by Equation 1.1, where *D* is the diameter of the sphere that encloses the antenna. Of the three regions, the reactive near-field region is the least predictable because it is dominated by reactive fields, resultant of the 90-degree phase difference between the E-field and H-field.

$$reactive\ near\ field \leq 0.62 \times \sqrt{\frac{D^3}{\lambda}} \tag{1.1}$$

The radiating near field region, also known as the Fresnel region, is predominated by radiating fields; however, reactive fields are still present in this region. The radiating near field region is defined as the region between the reactive and far-field regions (Equation 1.2).

$$0.62 \times \sqrt{\frac{D^3}{\lambda}} \leq radiating\ near\ field \leq \frac{2D^2}{\lambda} \tag{1.2}$$

Finally, the far-field region is the most commonly utilized region for antennas in a variety of applications due to its uniform fields. The far-field region is the most predictable field region of an antenna since the E-field and H-field are perpendicular to each other and in phase. The far-field region is defined as the region beyond the radiating near-field (Equation 1.3).

$$far\ field \geq \frac{2D^2}{\lambda} \tag{1.3}$$

The near-field regions are typically preferred for WPT because they are safer and more efficient; however, the transmission range is very short. The radiating near-field region is an interesting area of study in recent work in WPT [8]-[11] because the transmission range is longer than the reactive near-field, and it is more efficient and safer than far-field WPT. Therefore, radiative near-field WPT is explored in this thesis.

1.2 High Gain Antennas

For antennas operating the far-field region, directivity, gain, and realized gain are meaningful performance characteristics. Directivity is a measure of the peak radiated power divided by the average radiated power. The gain takes into account the antenna's efficiency by multiplying it to the antenna's directivity and realized gain takes the impedance matching into account by adding the mismatch factor. Therefore, directivity, gain, and realized gain are all proportional to each other.

High gain antennas are often preferred in many applications, as they can provide more extensive power to the receivers over longer distances. Some commonly used high gain antennas include parabolic antennas, helical antennas, horn antennas, and Yagi antennas; however, in this thesis, the focus is placed on the Yagi antenna, due to its simple design structure and low fabrication cost.

The conventional Yagi antenna, Fig. 1.2, consists of a $\lambda/2$ dipole as the driver element. It achieves an increased gain by using parasitic elements (elements that are not directly fed). There are two types of parasitic elements – the director, which is slightly smaller than the driver, and the reflector, which is slightly larger than the driver. The director is a capacitive element placed in the front of the driver element, and multiple may be used in the Yagi antenna. By contrast, the reflector is an inductive element placed behind the driver, and there is usually only one in a Yagi antenna. The spacing between elements is an important design parameter because as the spacing between elements decreases, bandwidth and impedance matching are negatively affected.

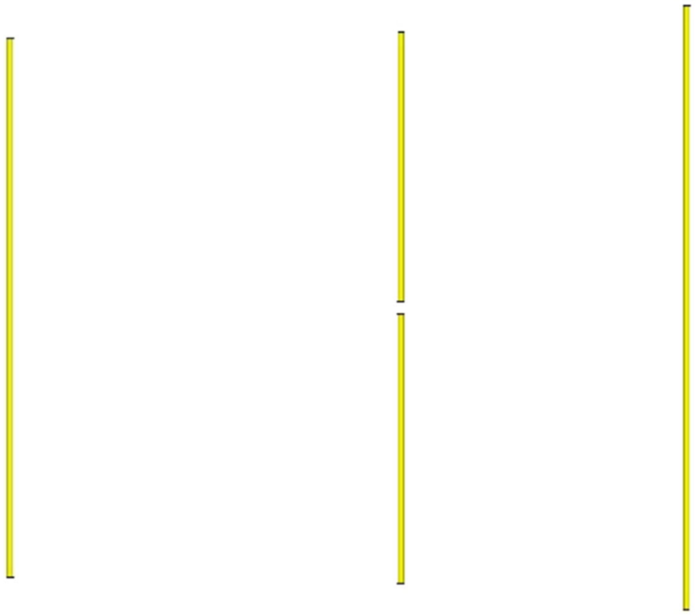

Fig. 1.2 The conventional $\lambda/2$ Yagi antenna.

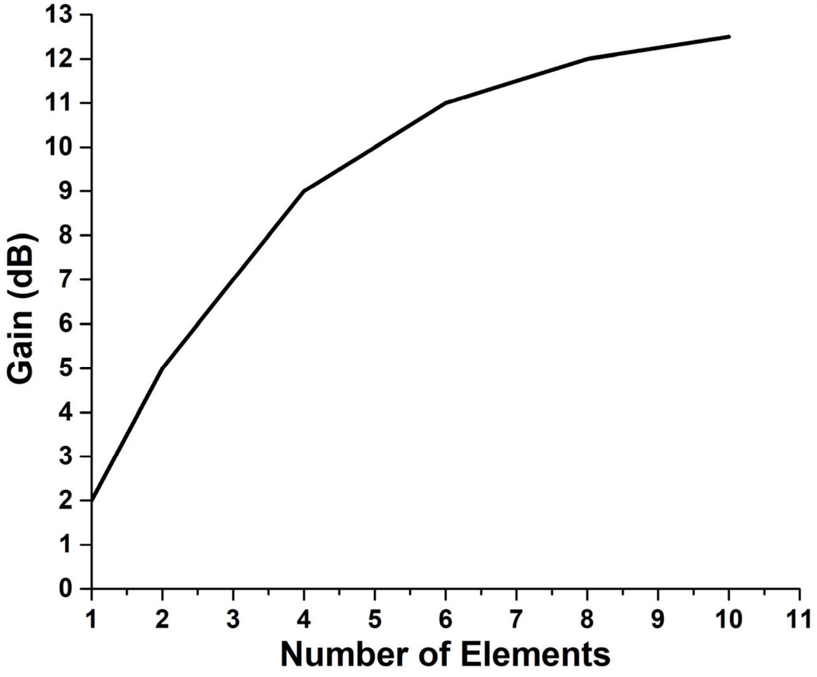

Fig. 1.3. Effect of an increased number of Yagi antenna elements on gain [12].

The number of elements may be increased, as shown in Fig. 1.3. As the number of elements increases, the antenna's gain is increased, which is proportional to the directivity [12]. Multiple directors are typically used to enhance directivity. The two-element Yagi antenna can utilize either a director or a reflector; however, the configuration using a director is more common.

Through an extensive literature search, it is found that although previous attempts have been made to reduce the size of the conventional Yagi antenna, [13]-[30], none achieve gain comparable to that of the full-sized, 15-element Yagi antenna. Additionally, reducing the size of an antenna results in decreased performance.

1.3 Electrical Size and Size-Reduction

In the antennas and wireless propagation community, it is common to refer to an antenna's size in terms of its electrical length and electrical size. These dimensions are based on the wavelength, λ, calculated at the operating frequency of the antenna. The electrical length is simply calculated by dividing the physical length by λ (Equation 1.4). The electrical size, *kr*, is calculated by multiplying the wave number, *k*, by the radius, *r*, of the smallest sphere which encloses the entire antenna, as demonstrated in Fig. 1.4 (Equation 1.5).

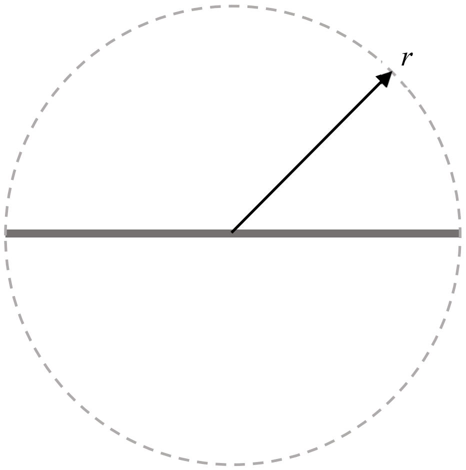

Fig. 1.4. The radius of the smallest sphere that encloses the antenna.

$$electrical\ length = \frac{length}{\lambda} \tag{1.4}$$

$$electrical\ size\ (kr) = k \times r = \frac{2\pi}{\lambda} \times r \tag{1.5}$$

An antenna is considered electrically small if the electrical size is less than 1, ($kr < 1$). As wireless devices' size is continually decreasing, the need for small antennas becomes more and more prevalent. Various size reduction techniques have been implemented in previous works. Two standard methods include folding and top loading. The folding technique demonstrated in Fig. 1.5 (a) is used to reduce the spacing between an antenna's elements. Typically, when interelement spacing is reduced, the radiation resistance decreases, and the antenna does not achieve good matching with the characteristic impedance of 50 Ω; thus, antenna performance is poor. The folding technique helps to steps-up the radiation resistance, to improve impedance matching [13]. In the top-loading technique (Fig. 1.5 (b)), the top-loading portion compensates for the reduced length of the vertical body, facilitating resonance at the desired frequency.

The top-loading method of size reduction has proven effective for maintaining bandwidth and efficiency in a reduced size, to an extent, which will be further discussed in this thesis.

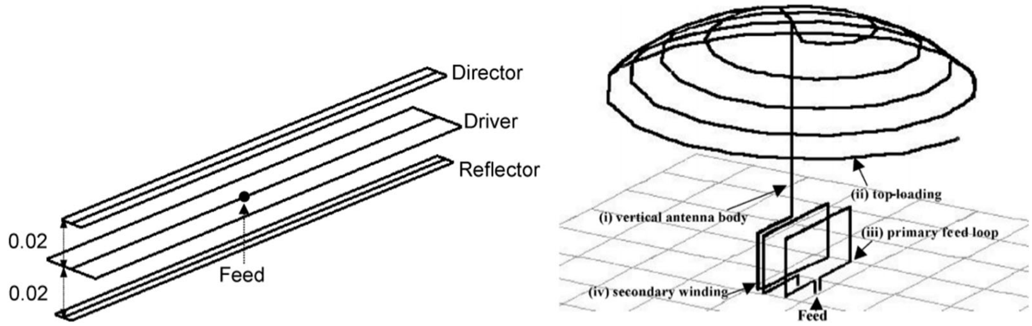

Fig. 1.5. Methods of antenna size reduction: (a) folding [13] and (b) top-loading [31].

1.4 Radio Frequency Identification

Radio frequency identification (RFID) is an ever-growing technology in everyday life. Although it has been around for a long time, it has become popular recently in endless applications, including tracking, localization, identification cards, use in credit cards and bus cards, etc. As researchers work to improve the read range and security of RFID systems, the list of possible applications continues to increase, including in road work and intelligent vehicles. There are two main types of RFID systems active and passive. Active RFID requires a power source (batteries) whereas passive, which will be focused on in this thesis, does not.

The main components of a passive RFID system are the tag antenna and the reader. The reader sends electromagnetic waves to the tag antenna, and if the tag antenna is within the reading range, it is activated, using WPT. Once activated, the tag antenna uses backscattering to send information back to the reader. This information includes a unique tag ID for identification and can also include a short message and password for security.

The tag antenna consists of an antenna geometry matched to an integrated circuit (IC) chip. The Higgs-3 RFID Tag IC, shown in Fig. 1.6 (a), is used in this work. It has 800-bit memory, is preprogrammed with a unique 64-bit serial number, has a low power requirement for reading and writing to the chip, and a reading range of up to 10m. The chip operates in the Ultra High-Frequency range (UHF), 902-928 MHz, and has an impedance of 20-j135 Ω within the bandwidth. Thus, the tag antenna must be designed with the conjugate impedance, 20+j135 Ω, for matching. Fig. 1.6 (b) shows the Alien 9662 tag antenna, which is a commercially available tag antenna. It has dimensions of 70 mm x 17mm and an omnidirectional radiation pattern. This antenna will be used as the reference antenna.

(a) (b)

Fig. 1.6. (a) Higgs 3 RFID chip and (b) commercially available RFID tag antenna.

In recent publications, many attempts have been made to increase the reading range of an RFID system by optimizing the design of the RFID tag antenna. In [32], an additional resonant coil is added in front of the tag antenna resulting in an increased reading range by a multiple of 2.7, from 16cm to 43cm. However, the resonant coil is very large, meaning that a large area is required for the RFID system even though the read range is only 43 cm. In [33], a recessed metal cavity is used to improve the reading distance by a factor of 1.7 compared to the ALN-9540 tag, achieving a 12.2m read range. An artificial magnetic conductor is placed on the bottom face of the cavity to reduce the height of the antenna.

1.5 Wireless Propagation Modelling

Although the design of a transmitter and receiver antenna is very important in the scheme of an effective wireless communication system, the wireless channel is another crucial factor of consideration. The wireless channel is the medium through which the electromagnetic waves sent from the transmitter must travel before being received by the receiver. Electromagnetic waves, also known as signals, may be transmitted between the antennas in five ways – line of sight (LOS), reflections, refractions, diffractions, or scattering. LOS communication occurs when there is a direct, unobscured path between the transmitter and receiver antennas. When a signal encounters an obstacle with a smooth surface, reflections and refractions occur, sending the signal in a different direction at an angle determined by Snell's Law. Scattering occurs when the surface of an obstacle is rough, resulting in multiple reflections and refractions in many directions. A signal may also bend around sharp corners of obstacles—diffraction. Non-line of sight (NLOS) communication occurs when reflected, refracted, diffracted, and/or scattered waves are received by the receiver antenna.

Propagation modeling is an empirical method by which researchers attempt to accurately characterize the behavior of electromagnetic waves as they travel within the wireless channel, taking into account the operating frequency, the distance between the antennas, presence and location of obstacles, etc. These models are quantified by the ratio of received power to transmitted power. Although Maxwell's equations may be used to accurately describe the channels, this procedure is tedious and requires extensive labor. Ray tracing is typically preferred, for its use of simple geometric equations. [34]

Wireless Insite is a 3D prediction software for the modeling of electromagnetic propagation using ray-tracing techniques. Using Wireless Insite, it is possible to accurately simulate a specific indoor or outdoor environment. It features an X3D propagation model that has no limits on antenna height or geometry and allows the importation of antennas designed in other software. It includes an extensive material library with electrical permittivity constants, for wood, foliage, concrete, dry and wet earth, etc. In this work, this software is used for all wireless propagation modeling simulations.

1.6 Thesis Objective

The objective of this thesis is to thoroughly investigate maximum wireless power transmission in a variety of applications. Firstly, various antenna geometries are compared to determine the optimal antenna design for radiative near-field WPT. Next, a directive, RFID tag antenna is designed to obtain a desirable read range for a pavement embedded application. The relationship between the Friis transmission equation, RSSI, and gain is investigated. A section of the Georgia Southern campus is investigated for maximum

GSM cellular coverage. Additionally, the genetic algorithm is used to optimize for maximum WIFI coverage in a residential home. Finally, a size-reduced Yagi antenna with gain comparable to the full-sized Yagi antenna with comparable bandwidth and efficiency, despite size-reduction is analyzed.

CHAPTER 2

ANALYSIS OF ANTENNA GEOMETRIES FOR NEAR-FIELD WIRELESS POWER TRANSFER

2.1 Introduction

As previously mentioned, there is an increased interest in radiative near-field WPT, for its increased transmission distance compared to reactive WPT and the increased power transfer efficiency and safety compared to far-field WPT. Recent works in radiative near-field WPT utilize a wide variety of antenna geometries. In [35], a WPT system is designed with a parasitic patch antenna with a gain of 8 dB as the receiving antenna and a patch array as the transmitting antenna. The system is optimized for maximum power transmission when implanted using a head model and attains a maximum transmission distance of 150 mm and PTE of 0.24% at the center frequency. In [36], both the transmitter and receiver are patch arrays; however, the transmitter is designed with Fresnel focusing (constructive interference at a specific point in the radiative (Fresnel) near-field region) by tuning the phase of each element in the array, and the receiver antenna is attached to a half-wave rectifier. This WPT system achieves an increased received power of 66.8% compared to a conventional beamforming array. In [37], electrically small antennas, including meander and helical antennas, are designed for radiative near-field WPT.

In [36], a table is provided comparing some commonly used antenna geometries, including the loop antenna, meander antenna, coil, and patch; but the comparison is insufficient to determine the optimal antenna geometry as the conditions in each publication are not consistent. The antennas operate at different frequencies with varying source powers and use different types of rectifiers or may not use any rectifiers at all. Thus, in this chapter, a selection of commonly used antenna geometries is designed at the same operating frequency, with the same source power, and without rectifiers. The effectiveness of these geometries in the radiative near-field is determined by an investigation of their in electrical field (E-field) strengths. The optimal antenna geometry for radiative near-field WPT is then determined based on the highest electrical field strength in the radiative near-field region.

2.2 Antenna Designs

Six different antenna designs, including those commonly used for WPT in the radiative near-field region, are designed for operation with at least -10-dB S_{11} at 2.4 GHz with a source power of 1 mW, and simulated in CSTMWS. These antenna geometries include the Archimedean spiral antenna, the patch antenna, and a meander antenna. Antenna geometries which are commonly used in the far-field region are also included. These far-field antennas include a full-sized dipole, full-sized, 3-element Yagi antenna, and a size-reduced, two-element Yagi antenna.

The Archimedean spiral antenna (spiral) consists of two arms, as shown in Fig. 2.1 (a). The number of turns, wire thickness, and spacing between the turns are tuned to obtain resonance with -10-dB S_{11} at 2.4 GHz. The antenna has an overall diameter of 37.7 mm (0.3λ), and five turns with a spacing of 2.6 mm between each turn. The antenna is designed using copper strips with a thickness of 0.26 mm. The Archimedean spiral has an electrical size of 0.95 kr.

The conventional patch antenna (patch) shown in Fig. 2.1 (b) is designed using the design equation (Equation 2.1) to determine the length of each side of the patch, where f_c is the center frequency, L is the length of each side of the square patch, ϵ_0 is the electrical permittivity constant in free space, μ_0 is the permeability in free space and ϵ_r is the dielectric constant of the substrate material (FR-4). The substrate has a thickness of 0.05λ. Copper is used for the patch and ground plane material.

$$f_c \cong \frac{c}{2L\sqrt{\epsilon_r}} = \frac{1}{2L\sqrt{\epsilon_0\epsilon_r\mu_0}} \tag{2.1}$$

Fig. 2.1, (c) and (d) show a full-sized dipole and full-sized, three-element Yagi antenna, respectively. The dipole is constructed with copper wire with a radius of 0.5 mm. The length of the dipole is approximately $\lambda/2$, after tuning for resonance with -10-dB S_{11} at 2.4 GHz. The full-sized dipole is used in the design of the full-sized Yagi antenna as the driver element, with the same approximate length of $\lambda/2$. Two parasitic elements (a director and a reflector) of similar copper wire with a radius of 0.5 mm are added with an inter-element spacing of 21.5 mm.

.

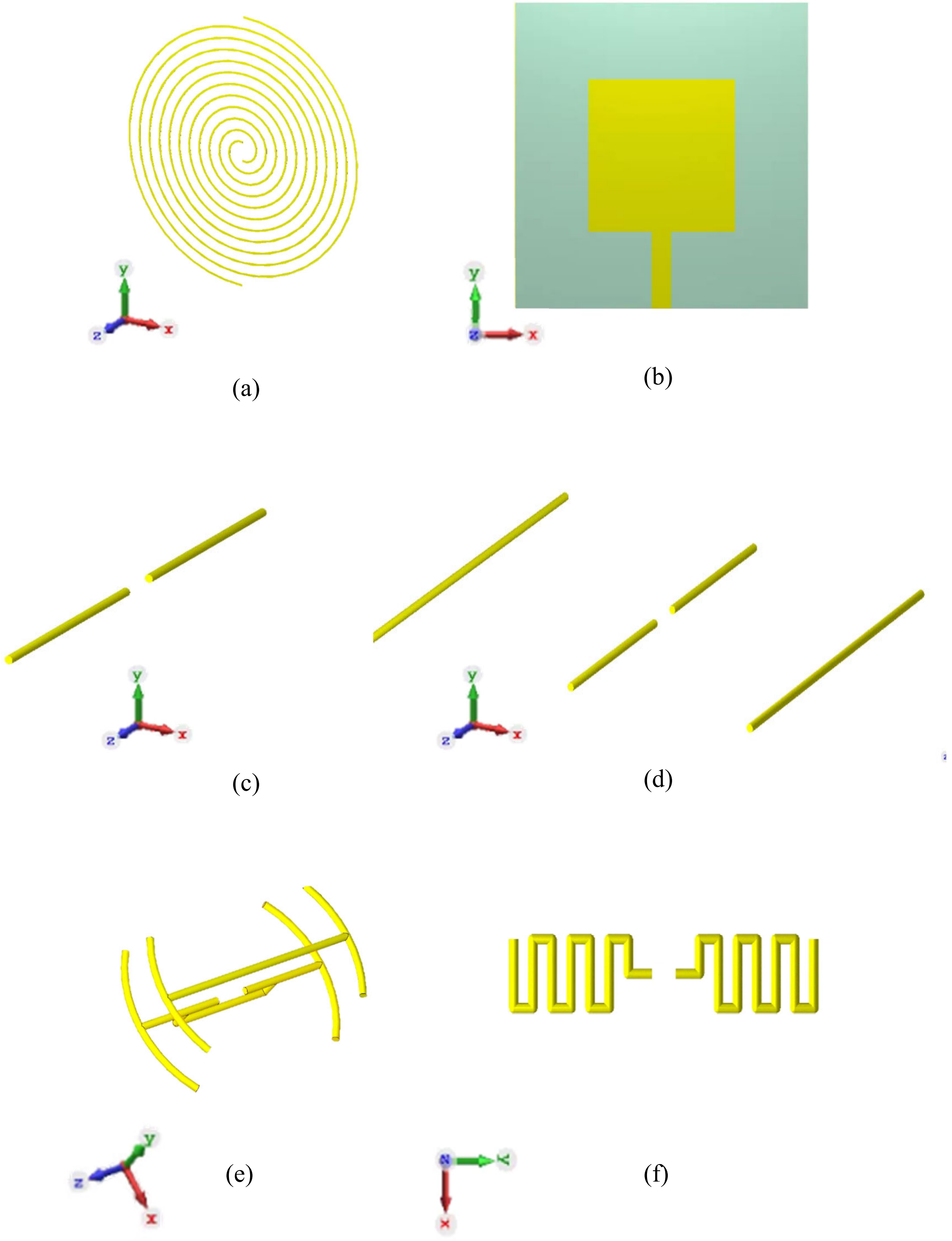

(a) (b)

(c) (d)

(e) (f)

Fig. 2.1. Antenna geometries investigated for radiative near-field WPT: (a) Archimedean spiral antenna, (b) patch antenna, (c) full-sized dipole antenna (d) full-sized, three-element Yagi antenna, (e) 0.8 *kr* directive antenna and (f) 0.8 *kr* meander antenna.

.

A size-reduced, 2-element Yagi antenna (0.8 *kr* directive antenna) is also designed using the rounded, T-shaped, top-loading method of size reduction, as shown in Fig. 2.1 (e). The antenna has an electrical size of 0.8 *kr,* and each element is constructed with copper wire of radius 0.5 mm. The interelement spacing between the driver and the director is considerably reduced to 7.6 mm compared with the interelement spacing of the full-sized Yagi. Thus T-matching on the driver element is required to improve radiation resistance for impedance matching at 2.4 GHz.

Lastly, a meander antenna (0.8 *kr* meander), shown in Fig. 2.1 (f), is designed with copper wire of radius 0.5 mm. The antenna has six turns with a spacing of 2.0 mm between each turn. The number of turns and the spacing between them are chosen by tuning for -10-dB S_{11} at 2.4 GHz while maintaining an electrical size of 0.8 *kr*. Similar size to the size-reduced, 2-element Yagi is desired since the radiative near-field region is calculated based on the longest length of the antenna (Equation 1.2).

2.3 Simulation Results

Fig. 2.2 shows the simulated S_{11} for each of the six antennas included in the study. As previously mentioned, each antenna has at least -10-dB S_{11} at 2.4 GHz. The patch and dipole antenna have the lowest S_{11} values at 2.4 GHz, due to better impedance matching with the characteristic impedance of 50 Ω.

The E-field strengths of each antenna are obtained from simulation for distances of 0 cm to 6 cm away from the front of the antenna and recorded in Fig. 2.3. The radiative near-field region of each antenna is calculated using Equation 1.2 and plotted in Fig. 2.3 with vertical dotted lines of the color corresponding to its plot for E-field strength. For example, upper and lower bounds of the radiative near-field region of the spiral antenna are indicated by the black, vertical dotted lines. It is observed that there is no common region where all of the antennas have overlapping radiative near-field regions. Thus, the antennas are split into two groups for analysis. Group 1 includes the spiral, the 0.8 *kr* directive antenna, and the 0.8 *kr* meander antenna. Group 2 includes the patch antenna, the full-sized dipole, and the full-sized, 3-element Yagi antenna.

.

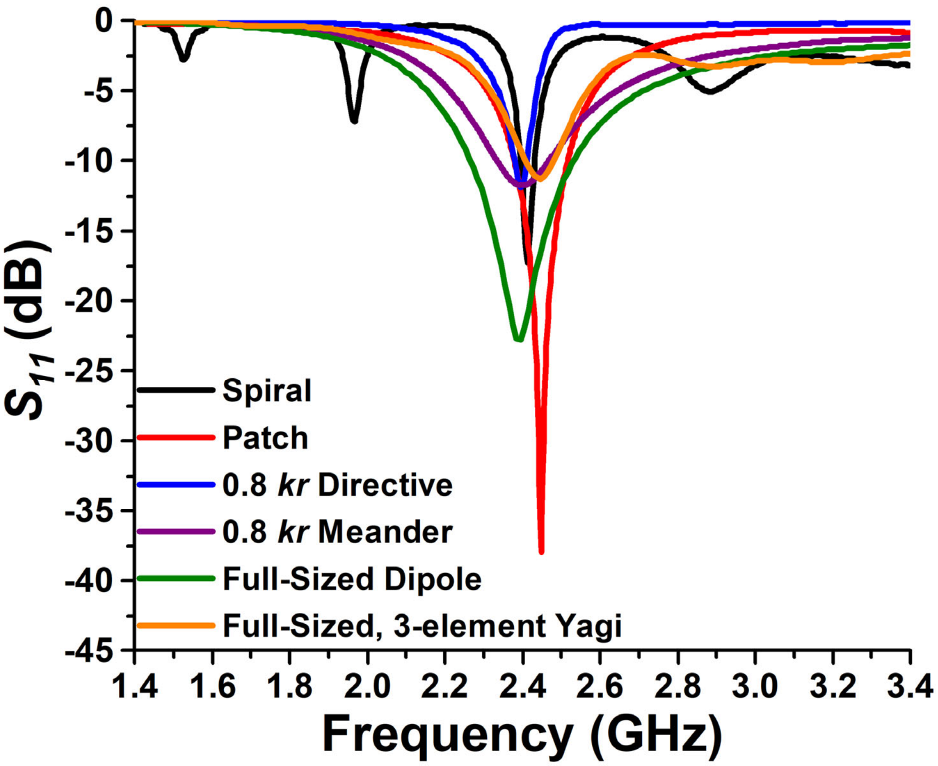

Fig. 2.2. Simulated S_{11} for the antenna geometries shown in Fig. 2.1.

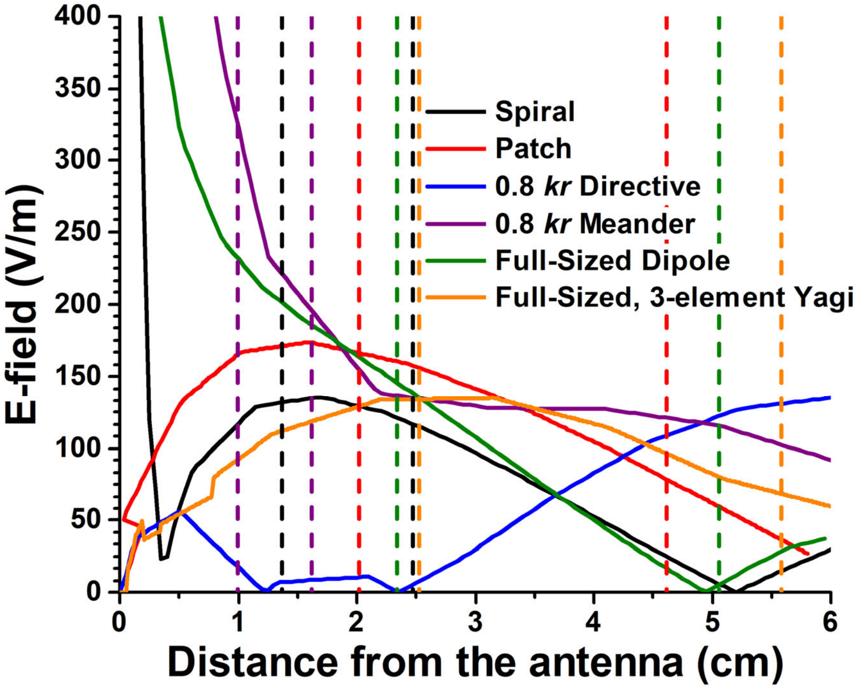

Fig. 2.3. Simulated E-field for the antenna geometries shown in Fig. 2.1.

.

The E-field for each antenna in group 1 is plotted for distances within the overlapping radiative near-field, in Fig. 2.4. Contrary to expectations based on the performance in the far-field, where an antenna with higher gain outperforms one with a lower gain, the 0.8 *kr* directive antenna has the worst performance in the radiative near field region. Therefore, far-field characteristics are not valid in the radiative near-field region. The meander has the best performance in this region, with the highest E-field strength of 200-220 V/m. It is followed by the spiral antenna with an E-field strength of 132-137 V/m. This is also unexpected since the meander antenna does not perform well in the far-field region due to current cancellations.

The E-field for each antenna in group 2 is plotted for distances within the overlapping radiative near-field, in Fig. 2.5. The patch antenna begins with the highest E-field values, but it is quickly surpassed by the Yagi antenna. This is because as the observation point is moved further and further away from the antenna, the far-field characteristics begin to come into effect, as shown by the E-field. Since the Yagi antenna has the highest gain, it is expected to have better performance in the far-field region.

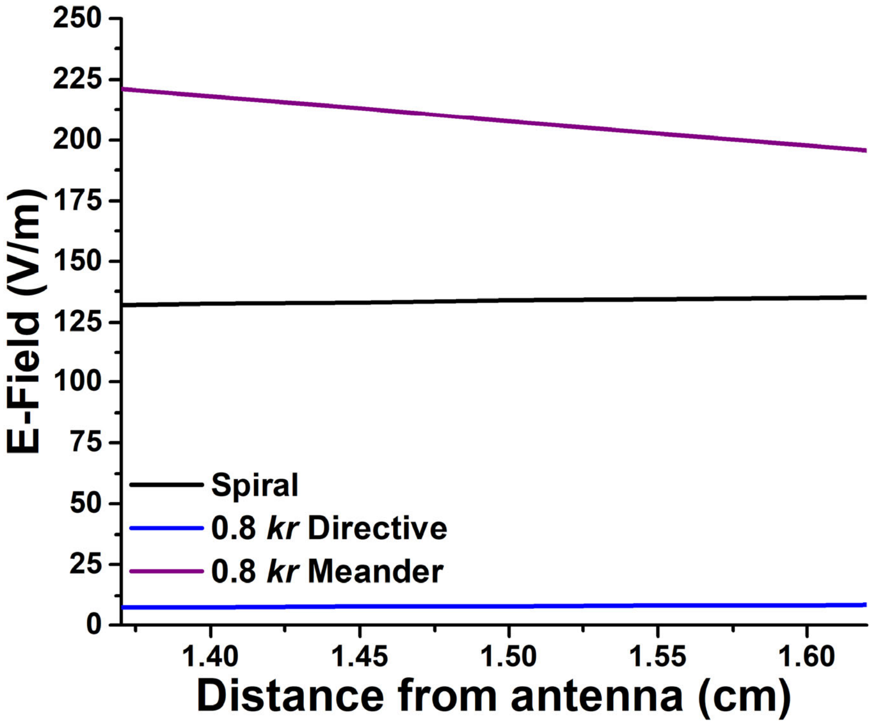

Fig. 2.4. The E-field for the antennas included in group 1: the spiral antenna, 0.8 *kr* directive antenna, and the 0.8 *kr* meander antenna.

.

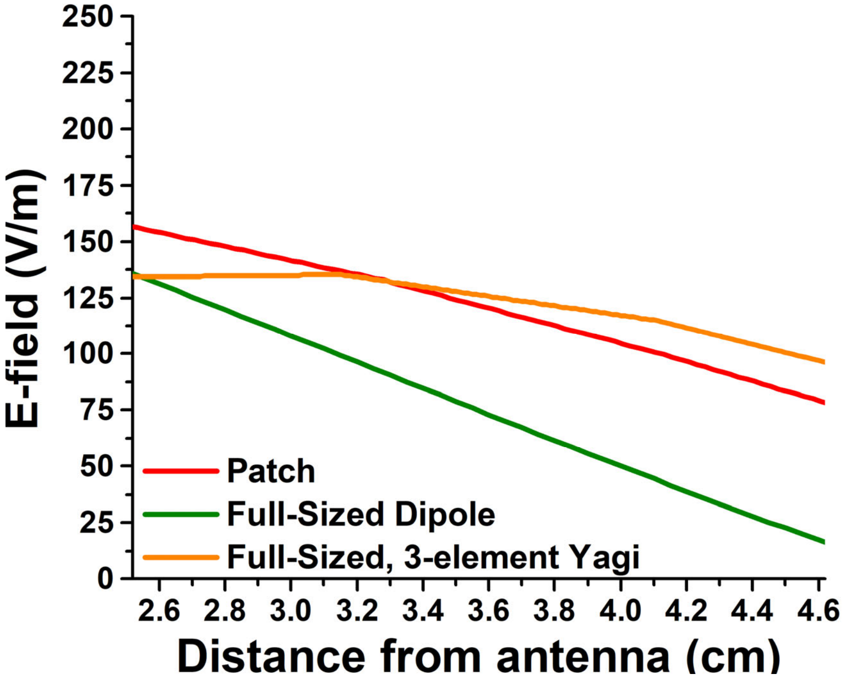

Fig. 2.5. The E-field for the antennas included in group 2: the patch antenna, the full-sized dipole, and the full-sized, 3-element Yagi antenna.

Overall, the meander antenna has the highest E-field values in its radiative near-field region. Thus, it is concluded that the meander antenna is the optimal antenna geometry for radiative near-field WPT.

2.4 Summary

Radiative near-field WPT has become an interesting area of study for its improved safety and efficiency compared to far-field WPT and its increased transmission distance compared to reactive near-field WPT. In previous works, various antenna geometries are utilized under varying conditions of resonant frequency, source power, and use of rectifiers making determining the optimal antenna geometry for radiative near-field WPT difficult. In this work, antennas commonly used for radiative near-field WPT and some commonly used far-field antennas are compared in terms of their E-fields in the respective radiative near-field regions. These antennas include the Archimedean spiral antenna, the patch antenna, the full-sized dipole antenna, the full-sized Yagi antenna, a 0.8 *kr* directive antenna, and a 0.8 *kr* meander antenna. Of the six antennas included in the study, it is determined that the 0.8 *kr* meander antenna is optimal for radiative near-field WPT because it has the highest E-field value in its radiative near-field region.

.

In future work, measurement based on S_{21} is needed to verify simulation results. The meander antenna may be used in a focusing array by using different phases on each element to focus the radiated power to the desired focal point in the radiative near field to further improve the performance. The focused array can then be implemented in a WPT system to determine the power transfer efficiency.

.

CHAPTER 3

DESIGN OF A DIRECTIVE, UHF RFID TAG ANTENNA FOR PAVEMENT EMBEDDED APPLICATION

3.1 Introduction

Passive RFID systems have a large variety of applications; however, for this work, the focus is placed on the applications of road work, localization in the absence of GPS and eventually can possibly be used for a variety of applications in smart cars. These antennas can store information about the condition of the road, date of the last service, GPS coordinates, and for smart cars—lane information, traffic information, etc.

In [39], a pavement marker antenna is designed using a monopole antenna folded to fit on top of a pavement marker. The antenna has a conical radiation pattern, a directivity of 4.2 dBi, in the direction normal to the ground plane. The antenna has a maximum read range of 4.6 m on top of the pavement. However, since the life span of the pavement marker is very short, needing to be replaced every 2-3 years due to the exposure to the weather elements and vehicles, the pavement embedded RFID has become a common area of study. In [40], the commercial RFID tag antenna is embedded in the pavement and achieves a read range of only 0.4 m. Therefore, recent works investigate antenna designs with longer read ranges.

Since the commercial RFID tag is a dipole antenna and has an omnidirectional radiation pattern, half of its power is lost to the pavement when it is embedded. Therefore, the dipole antenna is not a good design for the pavement embedded application. As demonstrated in Fig. 3.1, when a directional antenna is used, the majority of the antenna's power is radiated upward, away from the pavement, and less power is lost it. In [41], a parasitic patch array is designed with a metallic cavity to improve the gain and radiation efficiency while embedded in the pavement. With its top exposed and the remains embedded in the pavement, the antenna has a read range of 12.8 m. In this work, a directional antenna is designed to achieve an enhanced read range in the pavement embedded application.

.

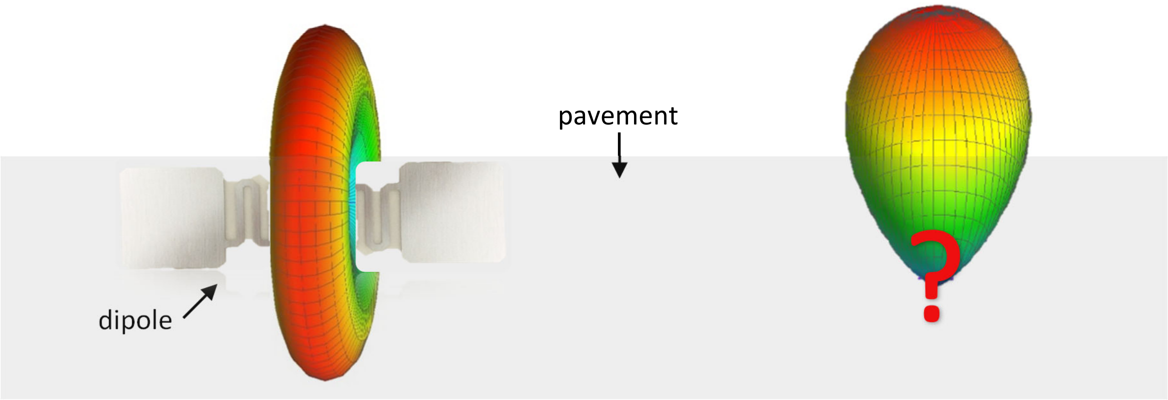

Fig. 3.1. Demonstration of an embedded dipole antenna with an omnidirectional radiation pattern versus an antenna with a directive radiation pattern.

3.2 Initial Antenna Design

3.2.1 Design Procedure

The initial antenna design is based on [13], where a closely spaced Yagi antenna is achieved through multiple folding technique implemented on the driver. The driver is constructed with copper wire with a radius of 0.5 mm and has two folds. A similar copper wire is also used for the director. The antenna design is rescaled for operation at 915 MHz and designed in FEKO. The main difference between the antenna design in [13] and the initial antenna is the location of the feed. The shifted feed is required to obtain impedance matching with the conjugate of the chip impedance.

A few parametric studies observing S_{11} are conducted by varying the feed location, driver dimensions, and interelement spacing to determine the initial geometry. The goal of the parametric study is to attain a directive antenna matched with the conjugate of the Higgs 3 chip impedance (20 + j135). Firstly, all dimensions are varied by scaling them with the variable, "*mult*", and the feed position is altered. The parametric study results are shown in Table I, and the best result is obtained when *mult* is 1.90, and the feed is 5mm away from the center of the driver. The resulting antenna design has a gain of 7.0 dBi and input resistance, R_{in}, of 30.51 Ω. Next, a closer study of the feed position was conducted to determine the feed location's effect on impedance matching. The results of the study are shown in Table II. Any slight

.

movement of the feed more than 0.5 cm results in a high capacitance (X_{in} drastically increases). Therefore 5 mm away from the center of the driver is chosen as the optimal feed position.

TABLE I

Parametric Study of *Mult* and Feed Location for S_{11}

Feed Displacement (m)	*Mult*	Frequency (MHz)	S_{11}
0.005	1.800	875	-4.500
0.005	1.895	920	-7.500
0.01	1.895	920	-12.30
0.01	1.850	905	-1.500
0.005	1.850	890	-1.980
0.005	1.870	905	-9.904
0.005	1.880	905	-2.234
0.005	1.885	905	-1.460
0.005	1.884	905	-1.635
0.005	**1.900**	**920**	**-12.33**
0.005	1.899	920	-12.33

TABLE II

Parametric Study of *Mult* and Feed Location for Input Impedance

Feed Displacement (m)	*Mult*	R_{in} (Ω)	X_{in} (Ω)
0.005	**1.900**	**30**	**128.6**
0.006	1.900	25	718
0.004	1.900	25	705

Lastly, a second variable, "*mult2*", is added to vary the spacing between the driver and the director elements, and a parametric sweep is implemented to manually tune the antenna. The resulting antenna design is shown in Fig. 3.2, having *mult* = 1.88, *mult*2 = 0.51.

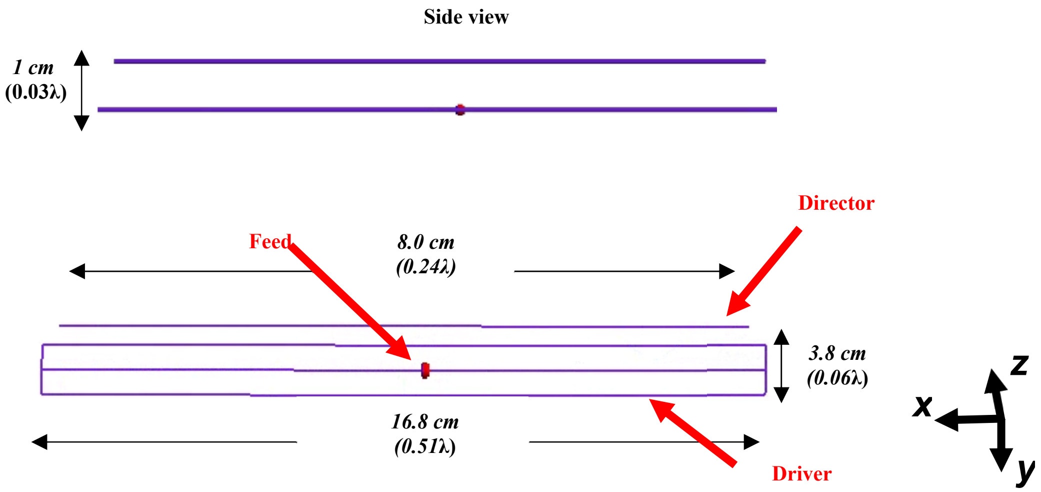

Fig. 3.2. Initial antenna design geometry.

.

3.2.2 Simulation and Measurement Results

As shown in Fig. 3.3, the antenna has a gain of 7.2 dBi in simulation. The initial antenna design has a minimum S_{11} of -23 dB at 913 MHz and an input impedance of 17.2 + j 149.2 Ω, as shown in Fig. 3.4 and 3.5, respectively. The -3-dB impedance bandwidth is 10% (905.4 – 918.3 MHz) and, unfortunately, does not cover the entire US UHF operating bandwidth for RFID antennas (902 – 928 MHz). The antenna, in fact, only covers 46.4% of the US required bandwidth. The antenna design is therefore modified to increase the bandwidth in the final antenna design.

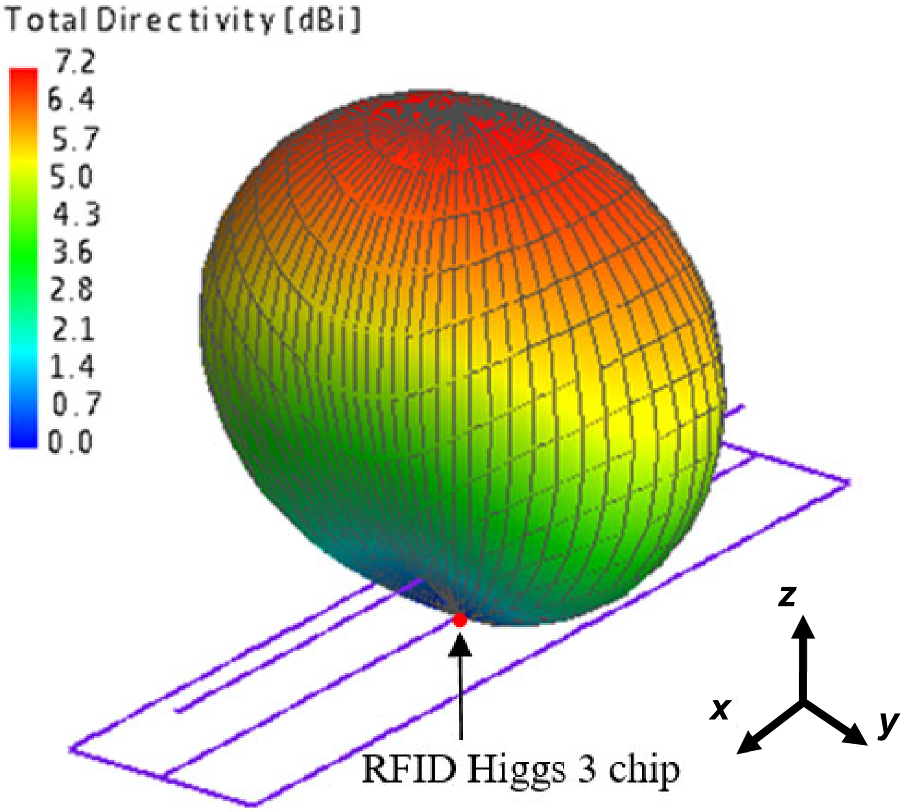

Fig. 3.3. The 3-D gain pattern for the initial antenna design.

.

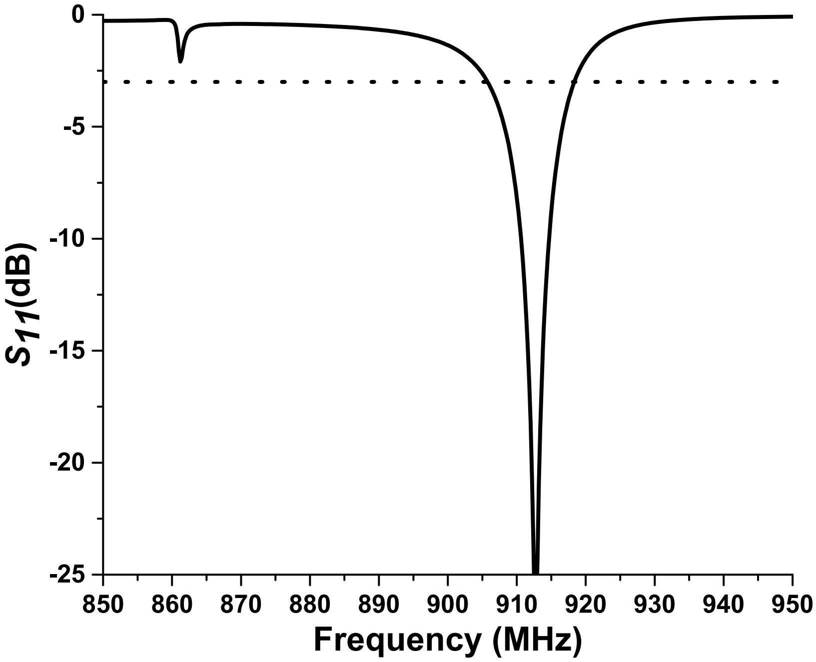

Fig. 3.4. Simulated S_{11} for the initial antenna design.

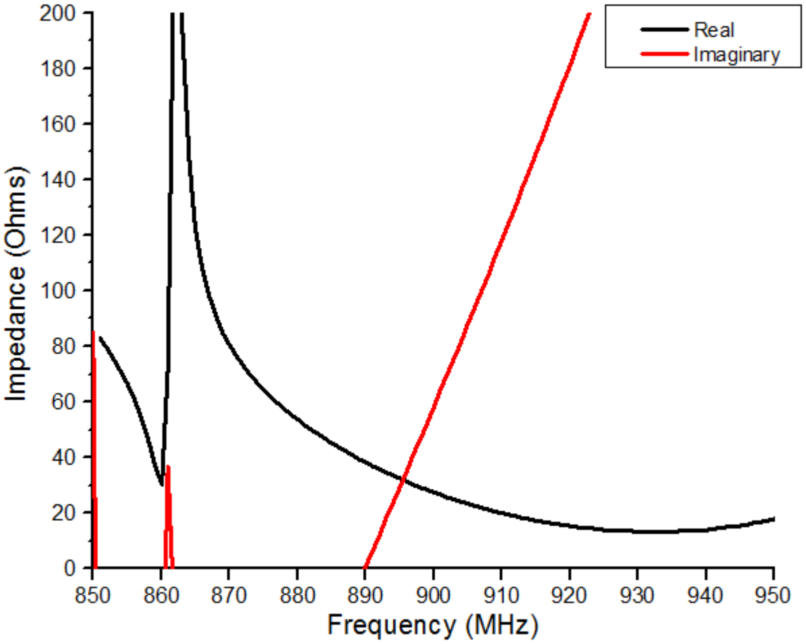

Fig. 3.5. Simulated input impedance for the initial antenna design.

.

The reading range is measured using a handheld reader. The antenna is set up 1m above the ground on a Styrofoam stand, and at every 10 degrees, the maximum distance that the reader is able to read information from the tag is recorded. For the initial antenna design, the maximum read range measurement is taken indoors, therefore any discrepancy may be a result of the indoor measurement environment or imperfect impedance matching. The antenna has a maximum read range of 8.9 ft in the direction of the director.

3.3 Final Antenna Design

3.3.1 Design Procedure

In attempts to achieve full coverage of the US UHF bandwidth, the director element of the initial antenna design is replaced with a wire bowtie element. The bowtie antenna is well known for broad bandwidth in a planar structure [7]. Each dimension in the antenna geometry is optimized for maximum realized gain at the resonance of 914 MHz and -3-dB impedance bandwidth over the 902-928 MHz frequency band. Compared to the previous iteration, a slightly larger interelement spacing is allowed, resulting in a reduced amount of folding on the driver. The GA optimized antenna structure is shown in Fig. 3.6. The antenna has a size of 0.49λ × 0.14λ × 0.05λ and thus can be easily buried. The feed is slightly offset from the center for impedance matching with the conjugate of the chip impedance, by 0.9 cm.

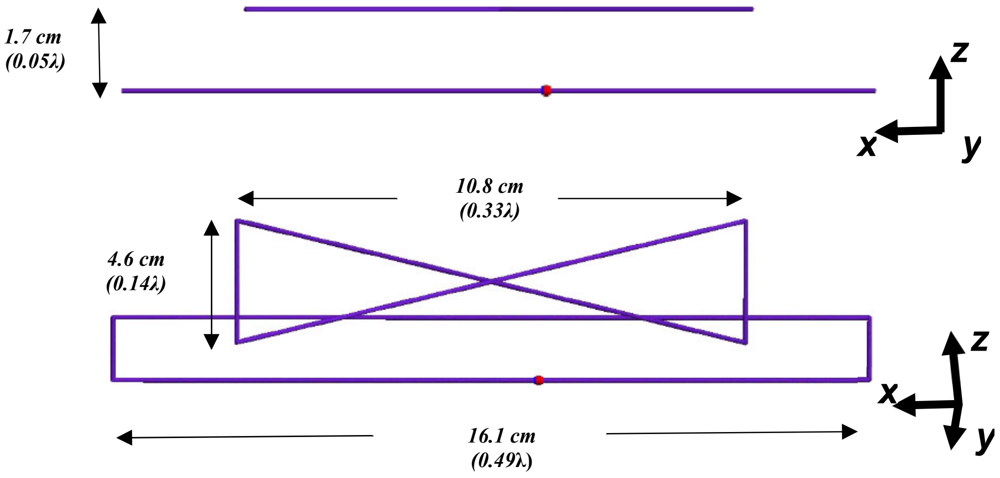

Fig. 3.6. The final antenna design for the UHF RFID tag antenna.

.

3.3.2 Simulation and Measurement Results

The final antenna design has a minimum S_{11} of -20.7 dB at 914 MHz, shown in Fig. 3.7. The -3-dB impedance bandwidth is 903-922.4 MHz, which is an improvement compared to the previous iteration. The final antenna design now covers 69.3% of the US required bandwidth (902-928 MHz) in simulation. The final antenna is fabricated for verification by measurement, as shown in Fig. 3.8. Copper wire with a radius of 0.5 mm is used to construct both the driver element and the director element. Styrofoam is used to support the antenna because it has a dielectric constant of 1.11, which is similar to that of air— thus, the effect of its proximity to the antenna is negligible. The measured S_{11} results agree well with the simulated S_{11}. In measurement, the antenna has a minimum S_{11} of -14.2 dB at 914 MHz. The -3-dB impedance bandwidth covers 72.1% of the US required bandwidth. The input impedance is also matched well to the conjugate the chip impedance (20 + j 135 Ω), both in simulation and in measurement – with a simulated value of 24.0 + j 135.6 Ω and a measured value of 13.4 + j 134.2 Ω at 914 MHz (Fig. 3.9).

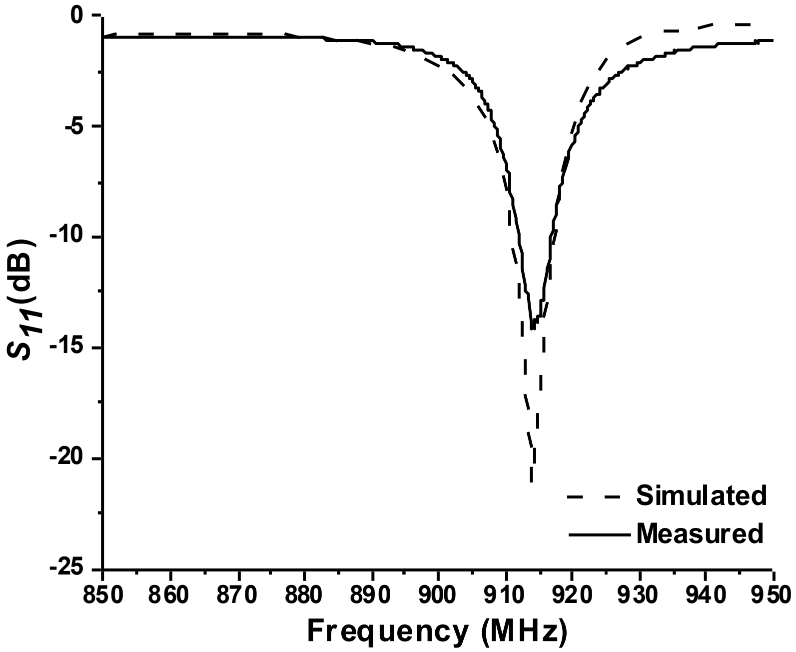

Fig. 3.7. Simulated and measured S_{11} for the final antenna design.

.

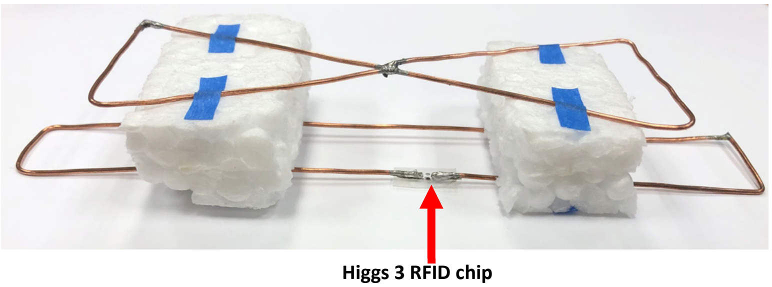

Fig. 3.8. The fabricated final antenna design for measurement.

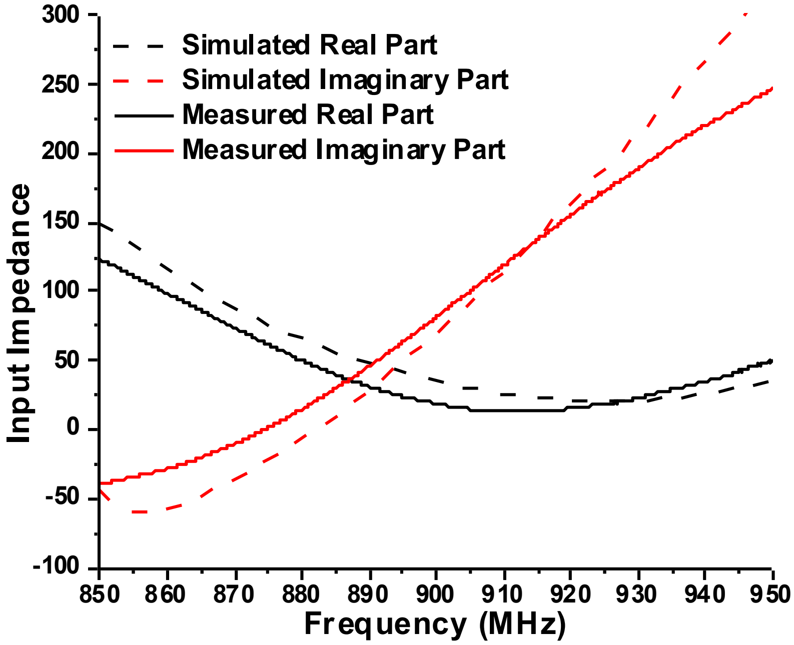

Fig. 3.9. Simulated and measured input impedance for the final antenna design.

The antenna has a maximum directivity of 7.38 dB as shown in the 3-D directivity pattern in Fig. 3.10. High directivity is achieved. The XZ and YZ realized gain patterns in Fig. 3.11 show that backward radiation is approximately equal to 0, verifying this. The plots also demonstrate a front-to-back ratio of 5 dB. It is observed that the radiation pattern is slightly tilted in the YZ plane, due to the feed offset.

.

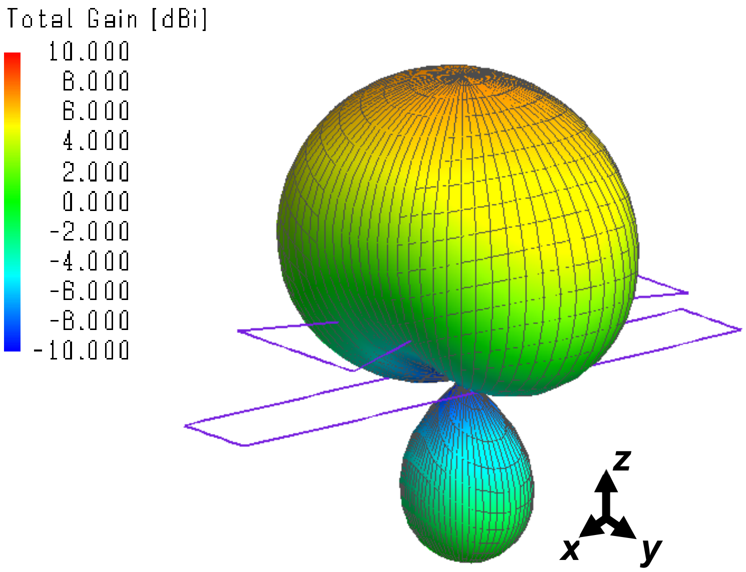

Fig. 3.10. The simulated 3-D directivity pattern for the final antenna design.

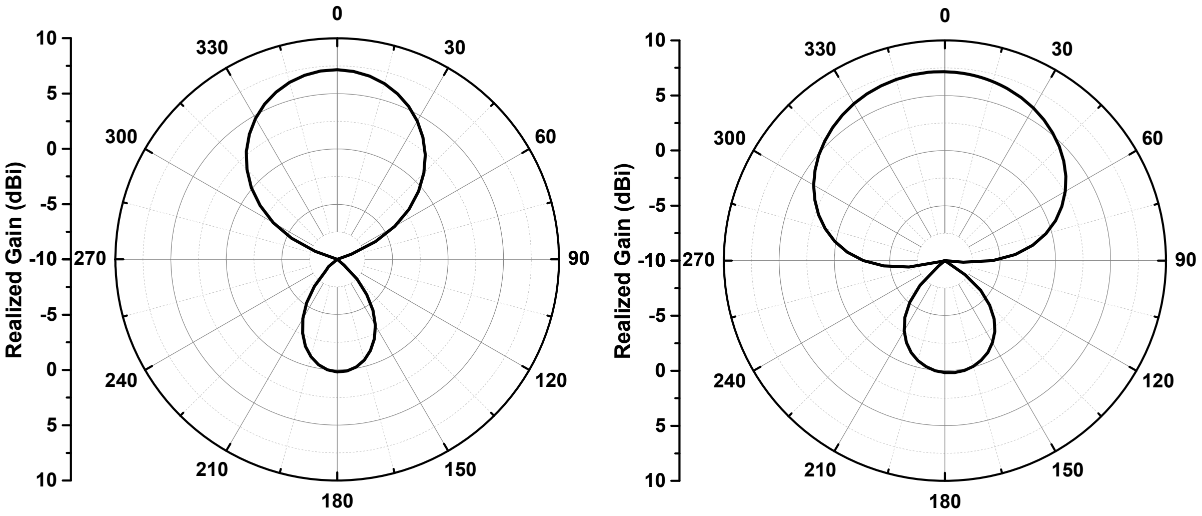

Fig. 3.11. The simulated realized gain patterns in the XZ-Plane and YZ-Plane, respectively.

Fig. 3.12 demonstrates the procedure for reading range measurement. Since the antenna is designed for the pavement embedded application, reading range measurements are taken with the antenna on top of the pavement. The antenna has a maximum read range of 14.2 ft (4.3 m) compared to the commercial RFID tag antenna, which had only 3.3 ft (1 m) maximum. The measurement is repeated for every 15 degrees to obtain the read range pattern shown in Fig. 3.13, which, as expected, is consistent with the radiation pattern

.

for the directive antenna and for the commercial antenna. The presented antenna is compared with the commercial antenna in Table III.

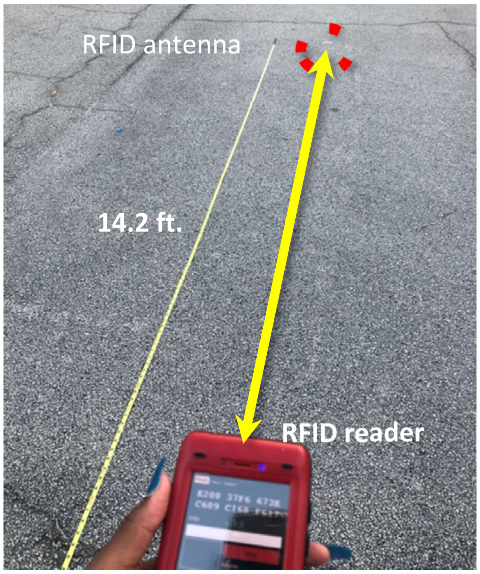

Fig. 3.12. Demonstration of the measurement procedure for reading range.

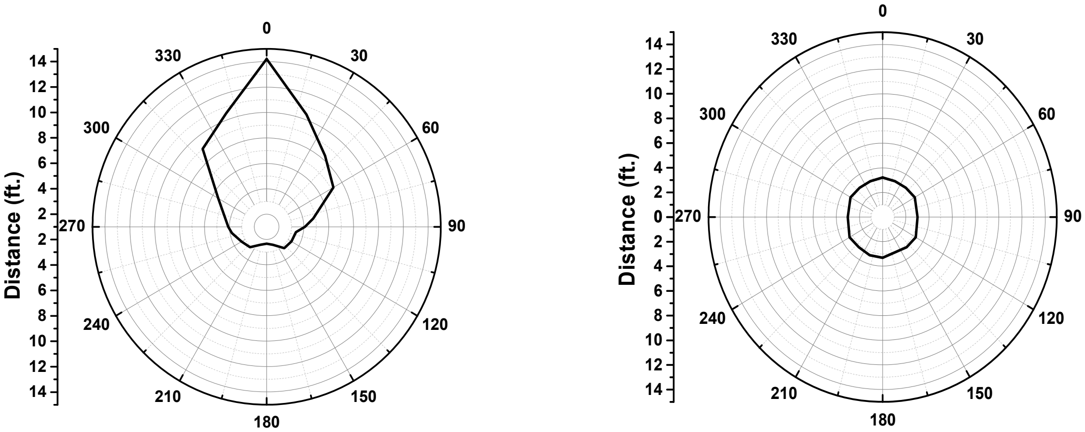

Fig. 3.13. Read range patterns for the final tag antenna design and the commercial tag antenna.

TABLE III
COMPARISON BETWEEN THE PRESENTED AND THE COMMERCIAL TAG ANTENNA

Antenna	Antenna Size	Read Range (Directly Above Pavement) (ft.)	Read Range (1m Above Pavement) (ft.)
Commercial	0.21λ × 0.05λ ×0.00 λ	6.0	10.0
Presented	0.49λ × 0.14λ × 0.05λ	14.2	47.0

.

3.4 Summary

A UHF RFID tag antenna is designed for pavement embedded application. It has an overall size of 0.49λ × 0.14λ × 0.05λ. The antenna is matched well to the conjugate of the RFID chip impedance and its bandwidth covers 72% of the US required bandwidth in measurement. Further bandwidth improvement can be obtained by using superposition of various bowties, in an overlapped fashion as the director element. The antenna achieves a directive radiation pattern with a directivity of 7.38 dBi in the direction of the director. The maximum reading range of the proposed antenna is 14.2 ft, compared with the 3.3 ft of the commercial antenna on top of the pavement. In future work, the behavior of the antenna when embedded into pavement should be taken into account.

.

CHAPTER 4

INVESTIGATION INTO WIRELESS PROPAGATION

4.1 Friis Transmission Equation

Path loss is defined as the power dissipated from electromagnetic waves travelling through a wireless network, from the transmitter to the receiver. The simplest path loss model is the Friis Transmission Equation, which is valid under the assumption of operation in free-space, line of sight communication, and polarization matching between the transmitter and receiver antennas (Equation 4.1). The Friis transmission equation relates the power received, P_r, by the receiving antenna to the power transmitted, P_t, by the transmitter, at a given distance between the two antennas [34]. D_t is the transmitter's directivity, D_r is the directivity of the receiver, λ is the wavelength at the operating frequency and d is the distance between the transmitter and receiver.

$$\frac{P_r}{P_t} = D_t D_r \left(\frac{\lambda}{4\pi d}\right)^2 \tag{4.1}$$

The Friis equation can then be simply modified to determine the power received by the receiver in dBm, as in equation 4.2, where power is in dBm and directivity is in dBi.

$$P_r = P_t + D_t + D_r + 20\log_{10}\left(\frac{\lambda}{4\pi d}\right) \tag{4.2}$$

For demonstration, received power is calculated using the Friis equation considering two conventional, half-wavelength dipoles operating at 914 MHz as the transmitter and receiver antennas. The distance between the antennas is varied between 10 m and 100,000 m, as illustrated in Fig. 4.1. Since path loss is a large-scale effect of wireless propagation, its impacts are better seen at distances far away from the transmitter. Dipoles have a typical directivity of 2.15 dBi, therefore this value is used for the calculation. The typical P_t of -30 dBm is also used. Using the same configuration in Fig. 4.1, a simulation is conducted in Wireless Insite for verification. Fig. 4.2 shows resultant the received power calculated using the Friis transmission equation and simulated in Wireless Insite Simulation. The results agree well and the received power decreases with r^2, as demonstrated by the slope of -20dBm.

.

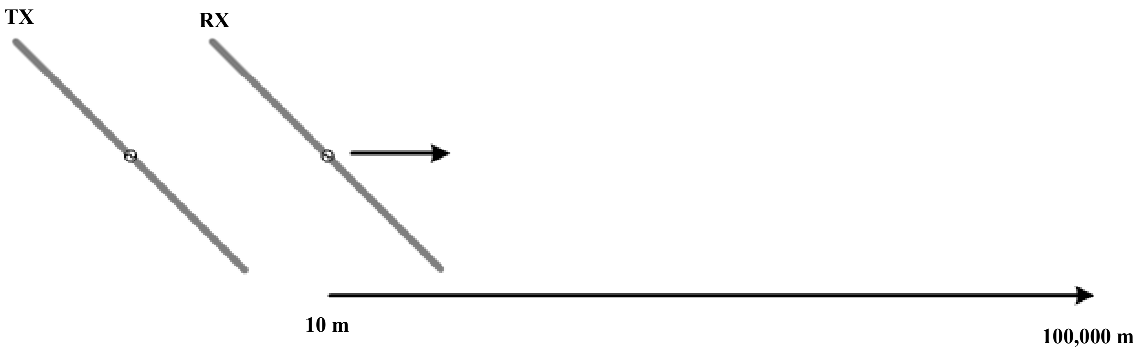

Fig. 4.1. Illustration of received power calculation for dipoles using Friis transmission equation.

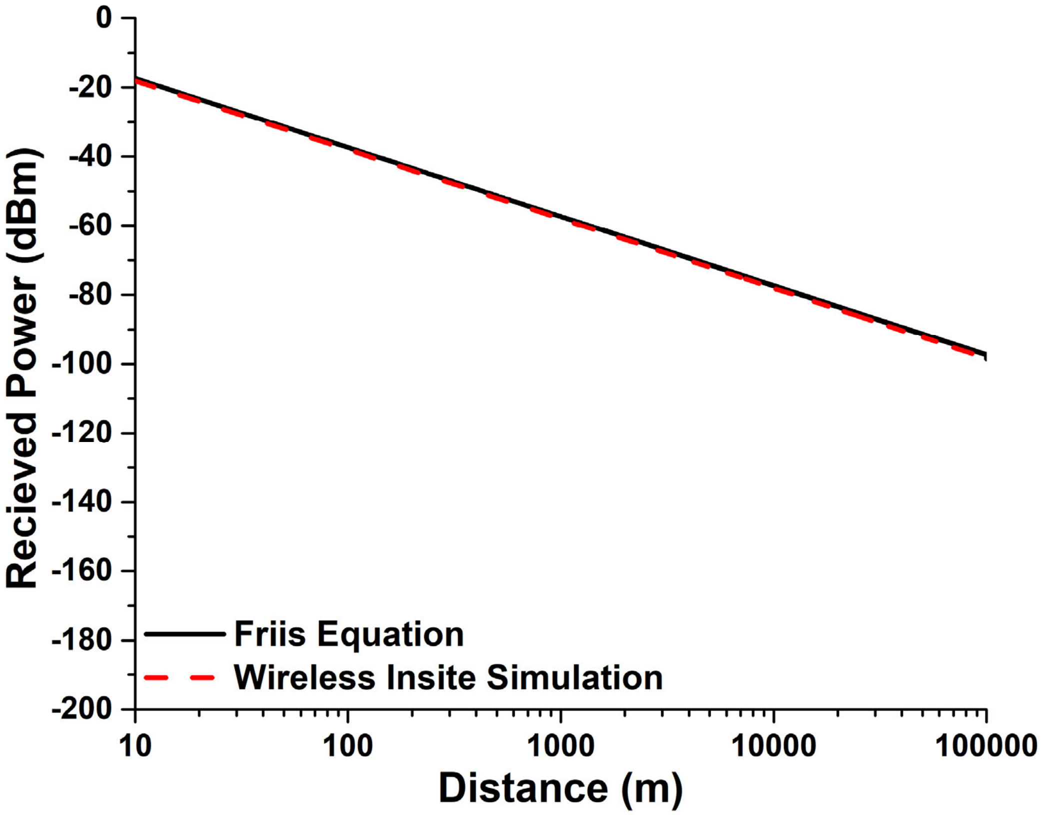

Fig. 4.2. Power loss for typical dipole antennas operating at 914 MHz calculated using Friis transmission equation.

.

The Friis Transmission equation deals with the ideal case, where the antenna is located in free space, however this generally does not apply in real-world applications. Received power is investigated in a few similar cases, where the antennas are instead located at distances of 1 m and of 10 m above dry earth and wet earth, as shown in Fig. 4.3. Compared to the free-space case, simulation above dry and wet earth yields a slight decreased received power. When the transmitter and receiver antennas are located 1m above both the wet earth and the dry earth, received power is similar. However, in the case where the antennas are located over wet earth, as the distance between the antennas increases, the received power is larger than in the dry earth case. Above earth, the slope is -40 dBm, meaning that the received power decays with r^4. The simulations with the antennas 10 m above dry and wet earth are approximately the same and demonstrate the presence of ripples in the received power. As previously mentioned, path loss is a large-scale effect on a signal. As the antenna height is increased, the effects of the reflections from signals interacting with the earth becomes more apparent.

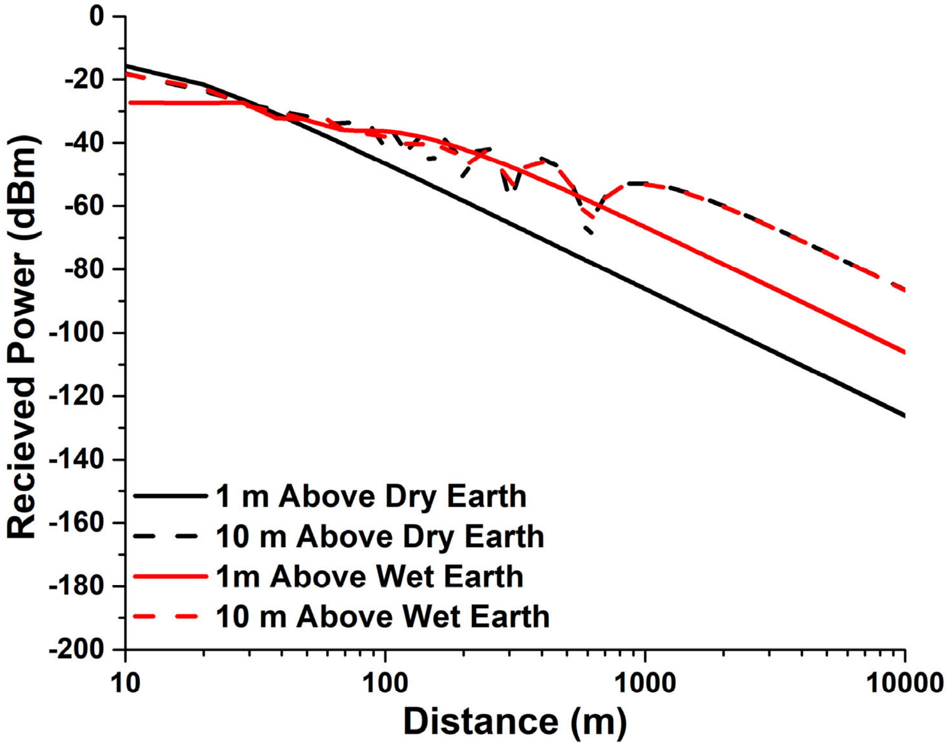

Fig. 4.3. Received power when antennas are located at 1 m and 10 m above wet earth and dry earth.

.

To demonstrate the relationship between received power and receiver gain, the simulation described in Fig. 4.1 is repeated, once more, with receiver gains of 5.0 dB and -5.0 dB. As shown in Fig. 4.4, the received power is directly proportional to the receiver gain. The slope of the received power versus logarithmic distance is maintained at -20 dBm for the various gain values. The difference between the received power using 5-dB gain and -5-dB gain is 10 dBm, at any distance between the two antennas. The difference in the received power between the 5-dB gain and 2.15-dB gain is approximately 3 dBm. Lastly, a received power difference of 7 dBm is demonstrated between the 2.15-dB and -5-dB gains.

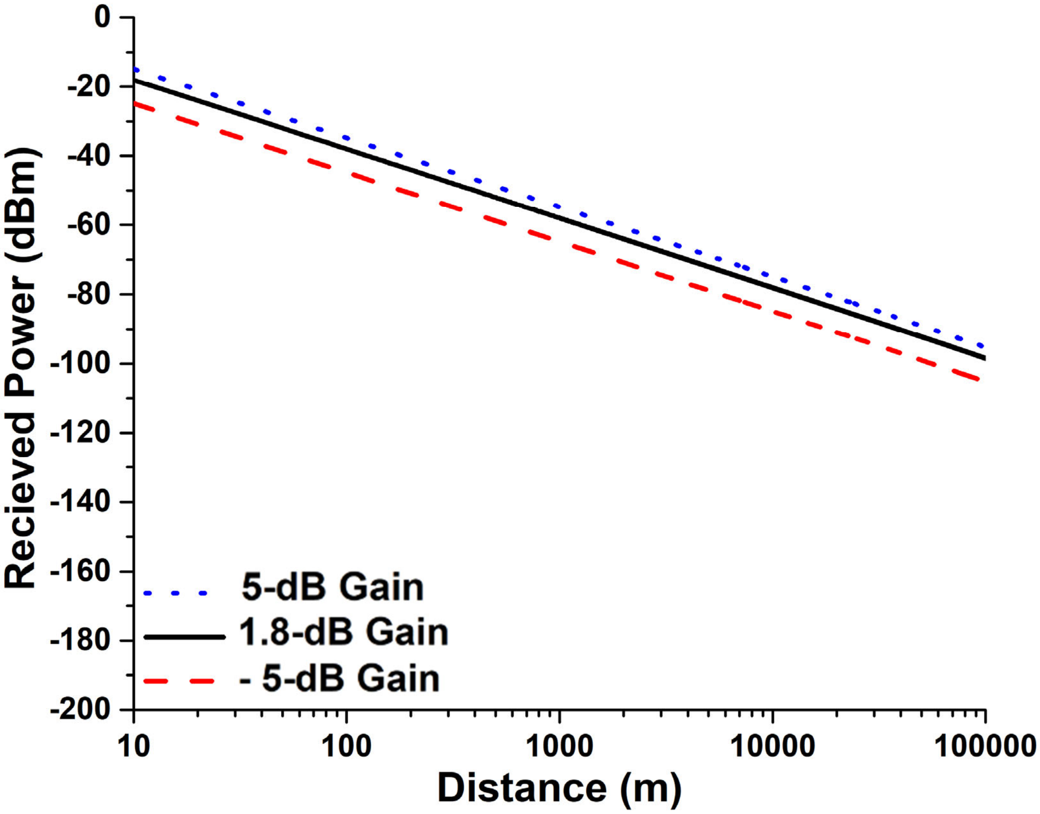

Fig. 4.4: Received Power for Varying Receiver Gain.

4.2 Maximizing Cellular Coverage on the Georgia Southern University Campus

4.2.1 Introduction

Originally designed for mobile terminals in vehicles, cellular phones have rapidly advanced and now a majority of the world’s population use the technology daily to communicate with others nationally

.

and worldwide and entertain themselves. The name cellular is derived from the operation of the system – the entire coverage area is divided into smaller cells, which are controlled by a base station (transmitter). Initially, large cells were used due to the high cost of constructing and maintaining base stations, which are usually to be constructed on the top of buildings or mountains and transmitted very high power, using omnidirectional antennas. Today, smaller cell sizes are more common, with base stations transmitting lower power due to necessity for an increased capacity and reduced price associated with base station construction and maintenance [34].

Since its commercial introduction in 1991, the GSM (Global System for Mobile Communications) has become the most commonly used cellular standard, with 900 MHz being the most frequently used frequency in the band. GSM has a bit rate of 270 kbps and provides short messages, cell broadcasting to users in a specific region, voice mail, call forwarding, data services etc. For a reasonable cellular signal, the cellular device's receiver must receive at least -87.5 dBm of power. For a great cellular signal ideal for uninterrupted streaming, -60 dBm received power is required at the cellular device's receiver.

On the Georgia Southern University campus, there is a cell tower located on the water reserve in front of the Performance Arts Center (PAC), as shown in Fig. 4.5. It is observed that cellular reception is lost in some areas on campus, for example around the Information technology building. In this work, this section of the university's campus is studied for maximum cellular coverage by implementing a cellular repeater to provide additional power to areas with weak signal. Using Google maps, an accurate model of the buildings' locations and sizes in the section of campus under investigation, is designed in and simulated Wireless Insite.

.

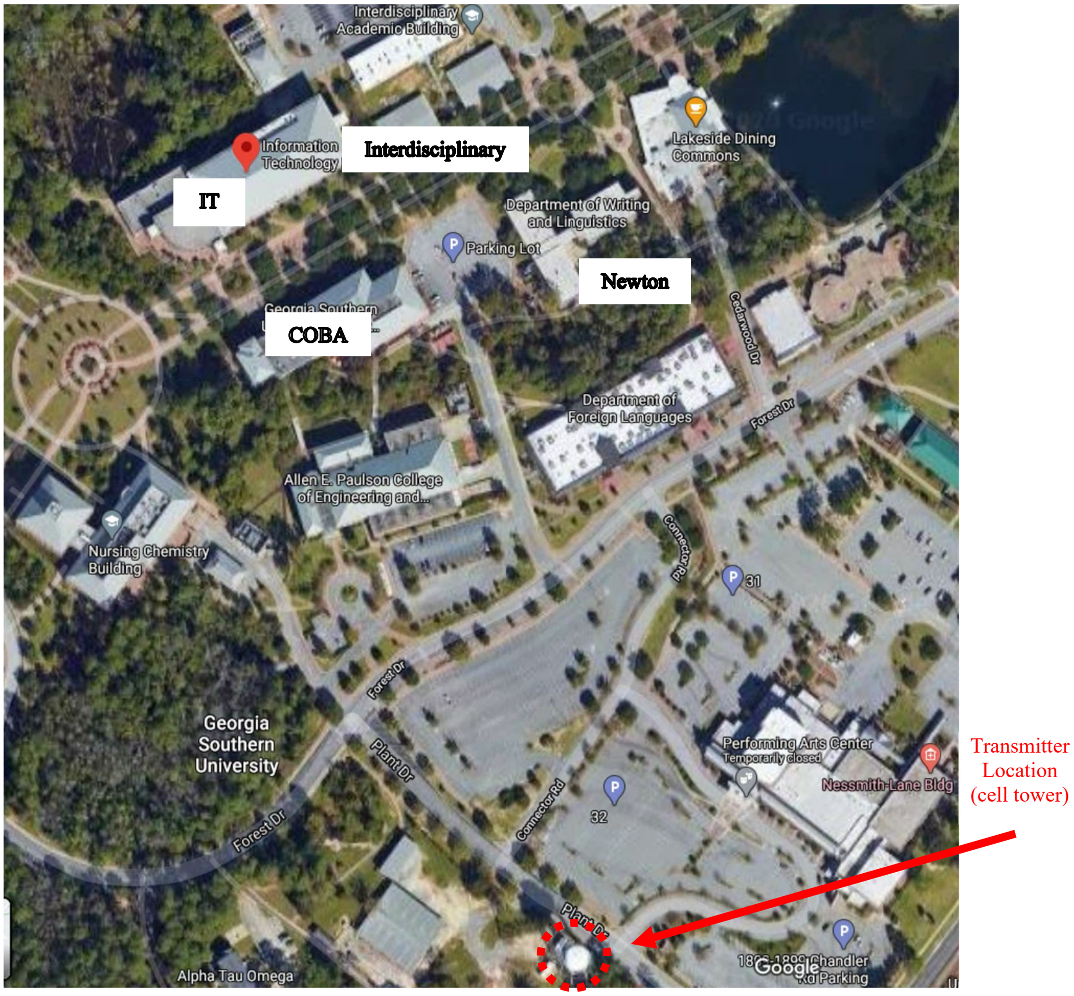

Fig. 4.5. Section of the Georgia Southern University campus under investigation.

4.2.2 Buildings Simulation

Fig. 4.6 shows the simulation framework. First, the transmitter antenna is designed in Wireless Insite at 900 MHz, which is the most frequently utilized GSM frequency. There are two primary antenna types used for cell towers: parabolic dish antennas and panel antennas. The antennas on the water reserve are panel antennas and are located near the top of the reserve to reduce the impact of obstacles and obtain a larger range of communication. From the data sheet of a commercial panel antenna, the gain of 8 dBi is chosen for simulation. The transmitter's location is acquired from the GPS coordinates in Google maps and the antenna height of 4 m is chosen since water towers are typically around that height.

.

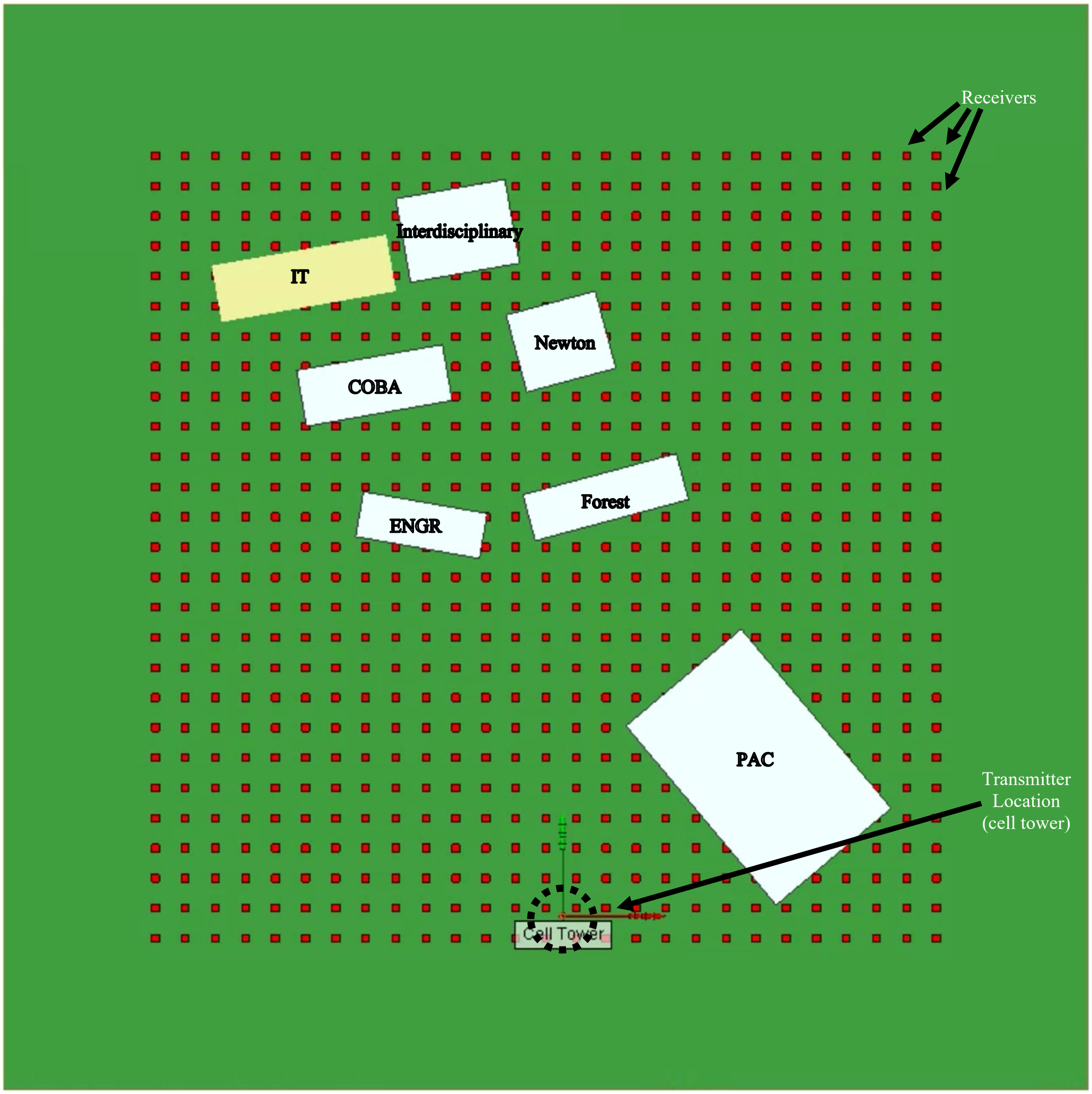

Fig. 4.6. Simulation framework for the cell tower and buildings in the area of investigation on the Georgia Southern campus.

Next the Information Technology (IT), College of Engineering (ENGR), College of Business (COBA), Department of Foreign Languages (Forest), Interdisciplinary, Department of Writing and Linguistics (Newton) and the Performing Arts Center (PAC) buildings are designed. Other buildings, for example the chemistry building, are neglected since they are directly in the area of study and thus have minimal effects on the area being studied (surrounding the IT building). Lengths and widths of the buildings

.

are accurately scaled, whereas building heights are estimated based on the number of stories. Each building is constructed using concrete material in simulation which has a dielectric permittivity of 15. Each surface has a thickness of 0.3 m, the default value provided for buildings in Wireless Insite. An evenly spaced grid of 729 receiver antennas with gain of 2.0 dBi is placed 1 m above the dry earth terrain.

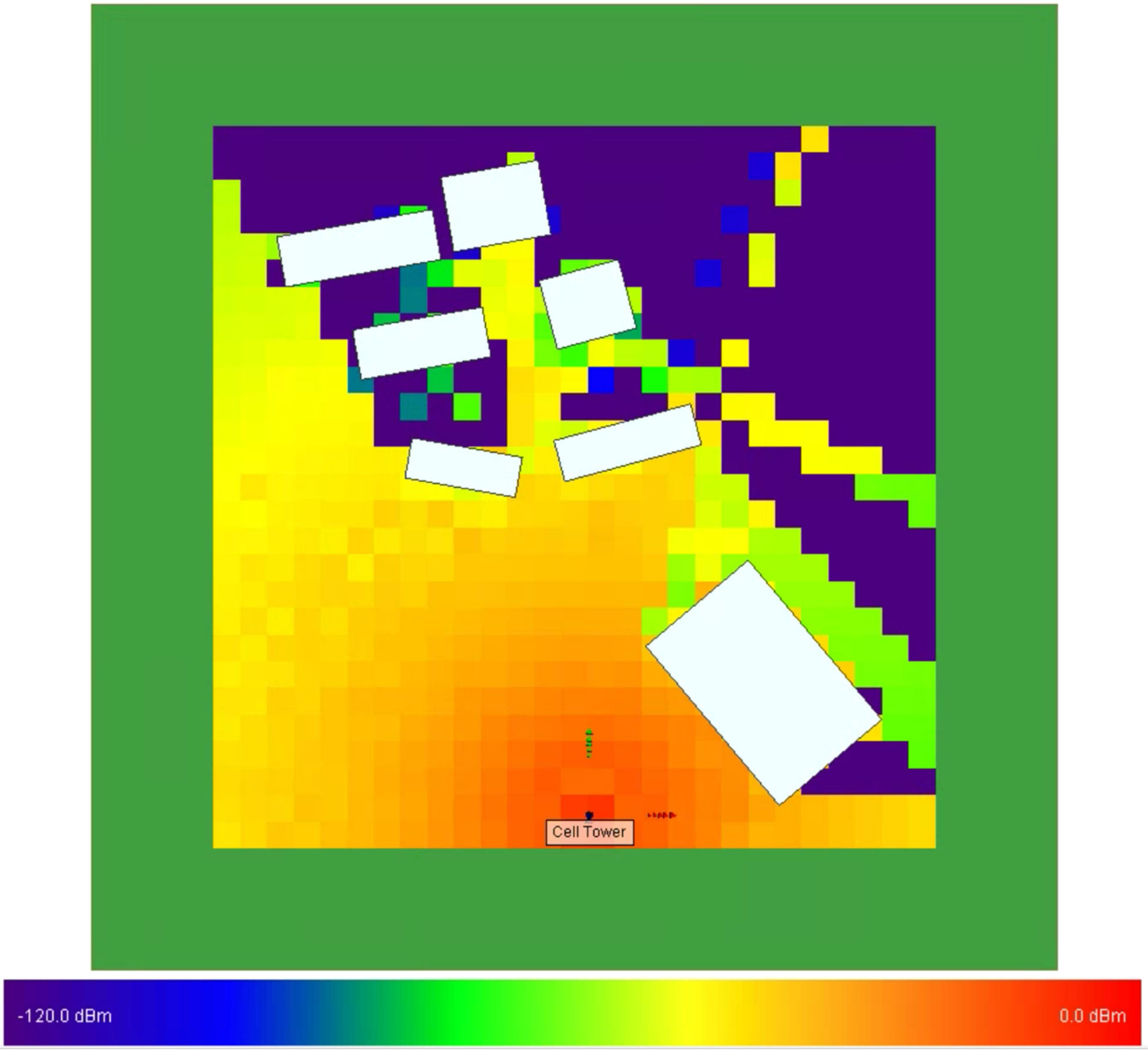

Fig. 4.7. Received power by a grid of receivers taking into account buildings in the area of study.

As shown in Fig. 4.7, the buildings obstruct line of sight in various locations in this area on campus, resulting in attenuated signal – this is referred to as shadowing. In [42], shadowing with respect to random objects in an urban environment, like pedestrians and cars, is investigated. This publication demonstrated

.

that the significance of the effects of shadowing depends on the obstacle's location with respect to the transmitter and the receiver. The authors of [43] use two independent random variables to model the effects of shadowing and path loss in 5G cellular networks, which is valid in a variety of cases. Various other publications investigate the effect of shadowing in a variety of applications, including in indoor environments and resultant from humans [44]-[46]. In the shadowed areas on campus, signal is lost when the received power is -120.0 dBm or less, and cellular coverage is not available in these areas. Some areas behind building still receive signal, with power values of about -60dBm, for example behind the PAC, due to diffractions around building edges and reflections. A poor signal or no signal at all is received at a total of 251 receiver points determined by using a MATLAB code written to count the number of receivers with received power less than -87.5 dBm.

4.2.3 Buildings and Trees Simulation

For a more accurate model, the large forested portions shown in Fig. 4.4, are adding to the simulation framework. The foliage feature (dense pine forest) in Wireless Insite is used with dielectric permittivity of 26. The average tree height of 15 m is used. The final simulation framework including the buildings, trees, cell tower and receivers is shown in Fig. 4.8.

The addition of the forested areas results in an increased received power value in some areas (in front of and behind the PAC, and on the right side of the Newton building) highlighted in Fig. 4.9. This results from reflections, diffractions and scattering, when the electromagnetic waves are met with the rough foliage surface. There are now less receiver points with inadequate signal. In [47], various models for propagation in forests of different densities are designed empirically. It was found that the signal attenuation is directly related to the density of the forest and diameter of tree trunks when the transmitter and receiver antennas under test are located inside of the forest. In this work, the focus is placed on the areas surrounded by forest. In [48], a method of modelling propagation through pine trees is investigated using multiple scattering, taking into account the impact of the bunch of needle-like leaves individually. Comparison with measurement confirms that the methodology works well for estimating behavior in pine forests. In [49],

.

resonant behavior in the forest is observed within specific frequency bands – less power is loss. This is also observed in [50].

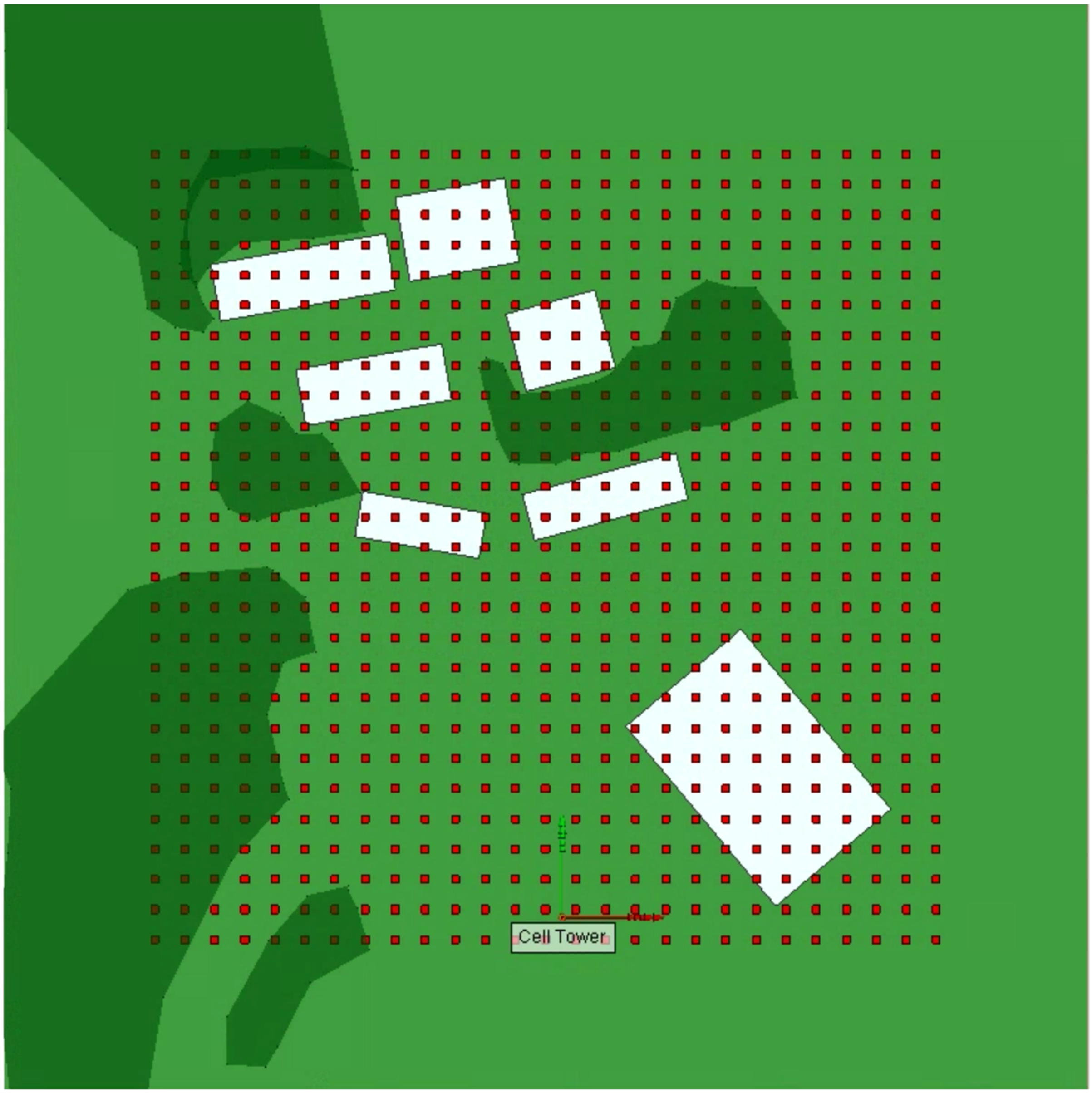

Fig. 4.8. Simulation framework for the area of Georgia Southern campus including trees.

.

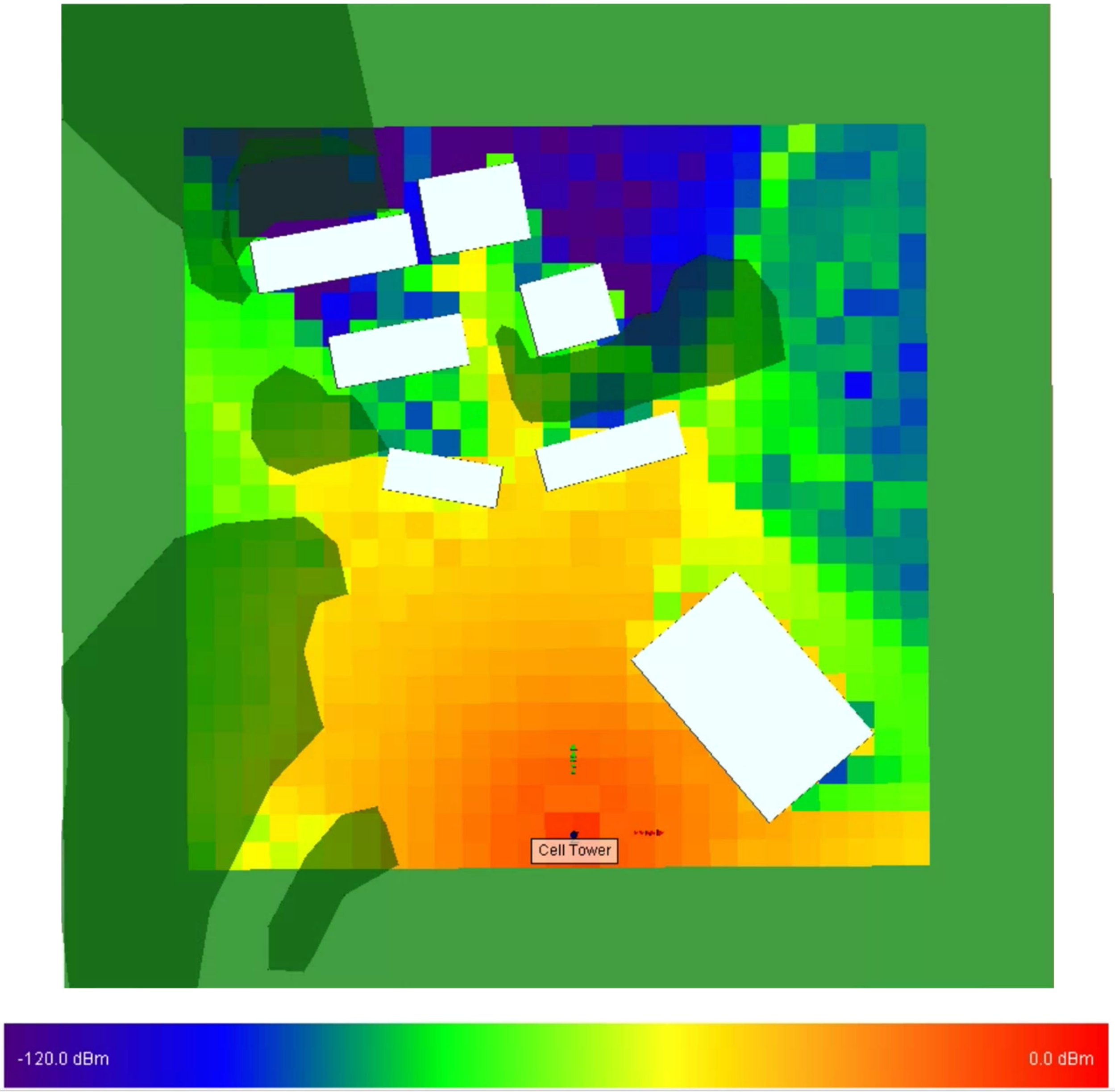

Fig. 4.9. Simulation results for the area of Georgia Southern campus including trees.

4.2.4 Implementation of Repeater for Maximum GSM cellular coverage

In attempts to improve the received signal in low signal areas in the section of campus in question, seven repeater locations are investigated. Repeaters are often used in cellular networks to extend the coverage range. The repeaters use the same antenna gain and height and are placed in areas of low signal.

.

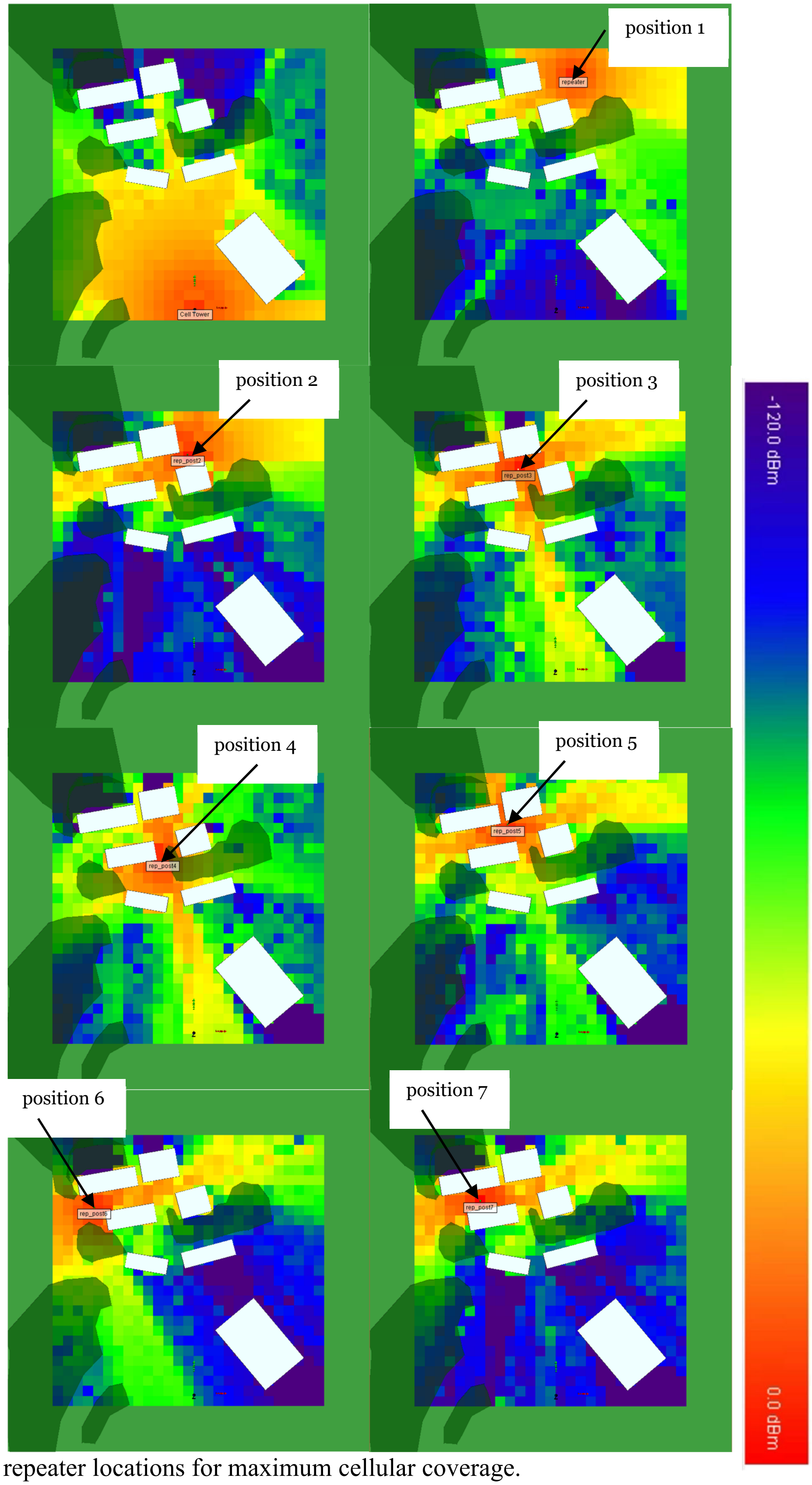

Fig. 4.10. Tested repeater locations for maximum cellular coverage.

.

The power received by the grid of receivers for each case is shown in Fig. 4.10. The cases without any repeaters is shown again in the top left for reference. In the top right is the power received by the receiver from the repeater is placed at position 1, and in the bottom left is the power received by the receivers when the repeater is placed at position 7. The total coverage, by both the cell tower and repeater, can be seen by overlapping the received power from both transmitters, however it is hard to decipher the best repeater location in this way. The results of a simple MATLAB code to count the number of receiver positions with inadequate signal (below -87.5 dBm) and average signal (below -60 dBm) are summarized in Table 4.1. In the base simulation framework, there are 251 receivers with inadequate received signal. The best results are shown when the repeater is located at position 1 and position 5. Although position 5 has the smallest number of receivers with power value less than -87.5 dBm, position 1 has the lowest number of receivers with power values less than -60 dBm — meaning that a better signal is received at more points on campus. An additional repeater may also be used to ensure full coverage.

TABLE IV
REPEATER POSITION COMPARISON

Repeater Position	Number of Receivers Below -87 dBm	Number of Receivers Below -60 dBm
x	251	288
1	**24**	**180**
2	26	200
3	27	210
4	29	258
5	**19**	**202**
6	38	209
7	31	213

4.3 Parallel Optimization for maximum WIFI signal in indoor environment

4.3.1 Introduction

In 2012, include the IEEE 802.11ad amendment was implemented, which provides a standard for 60 GHz for WIFI operation. The 60 GHz WIFI frequency allows high data transmission rates, over short distances. Additionally, it is difficult for high frequency waves to penetrate materials, like walls, furniture etc. Therefore, study is needed to determine the behavior in specific cases. Indoor propagation modelling

.

is commonly studied to observe WIFI behavior indoors, since each indoor environment is different. Empirical modelling methods may be used however, this requires excessive work in taking measurements. Ray-tracing methods have proven effective with a greatly reduced workload. In [51], a site-specific ray-tracing model is paired with genetic algorithm (GA) optimization to obtain full coverage with varying number of transmitters.

In this work a specific home environment is studied. Using genetic algorithm, the optimal transmitter position is determined using Wireless Insite ray-tracing and parallel Genetic Algorithm optimization.

4.3.2 Simulation Framework and Results

The area of interest is a residential home located in Statesboro, Georgia. It is a two-story building with four bedrooms, a living room and kitchen. The home is constructed in Wireless Insite, as shown in Fig. 4.11, where the bottom floor is on the left, and the top floor is on the right. The outer walls are constructed with concrete material, with electrical permittivity of 15.0, and each floor has a height of about 3.0 m. The inner walls are constructed with layered dry wall material (electrical permittivity of 2.8 on the outer surfaces and 1.0 on the inside. Furniture is also designed with the similar material types corresponding to the actual objects, for example, the coffee table uses wood material with electrical permittivity of 5.0.

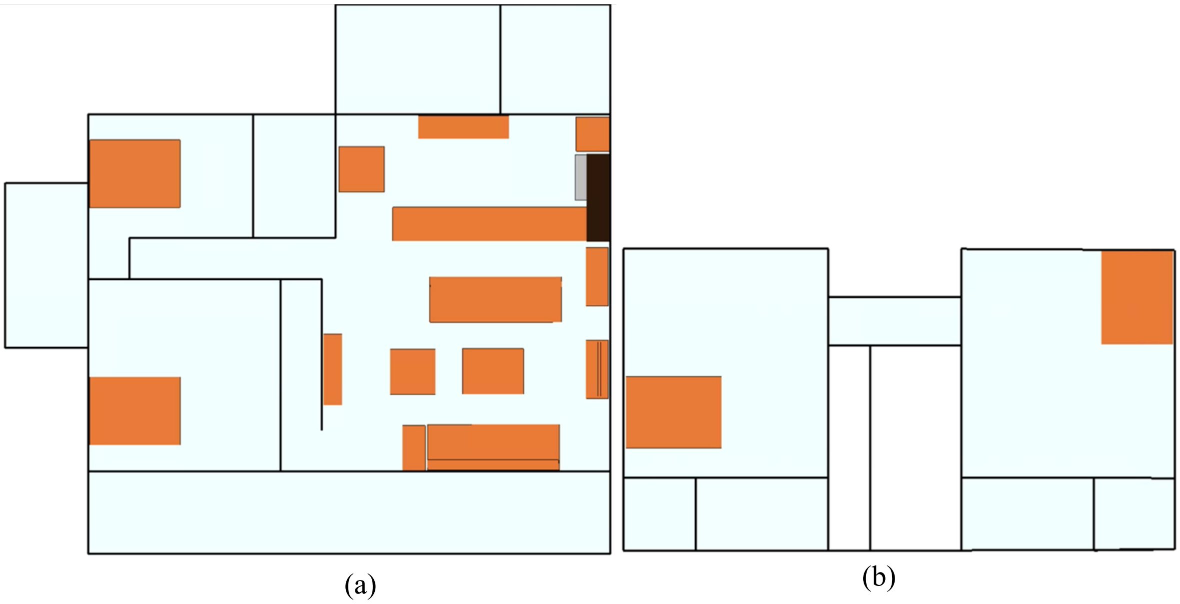
(a) (b)

Fig. 4.11. Simulation model for (a) the bottom floor and (b) the top floor of a residential home.

.

A 32×32 patch array antenna operating at 60 GHz is used for the transmitter and the receiver antennas. A grid of 87 receivers located 1 m above the ground, is used to cover the entire floor plan of the home, as shown in Fig. 4.12. This is done so that the received power at all points in the home can be investigated. The transmitter is located on the ceiling of the bottom floor, 2.7 m above the ground and is always oriented with its frontside directed toward the center of the room. The position of the transmitter is altered continuously to determine the optimal location for the best coverage.

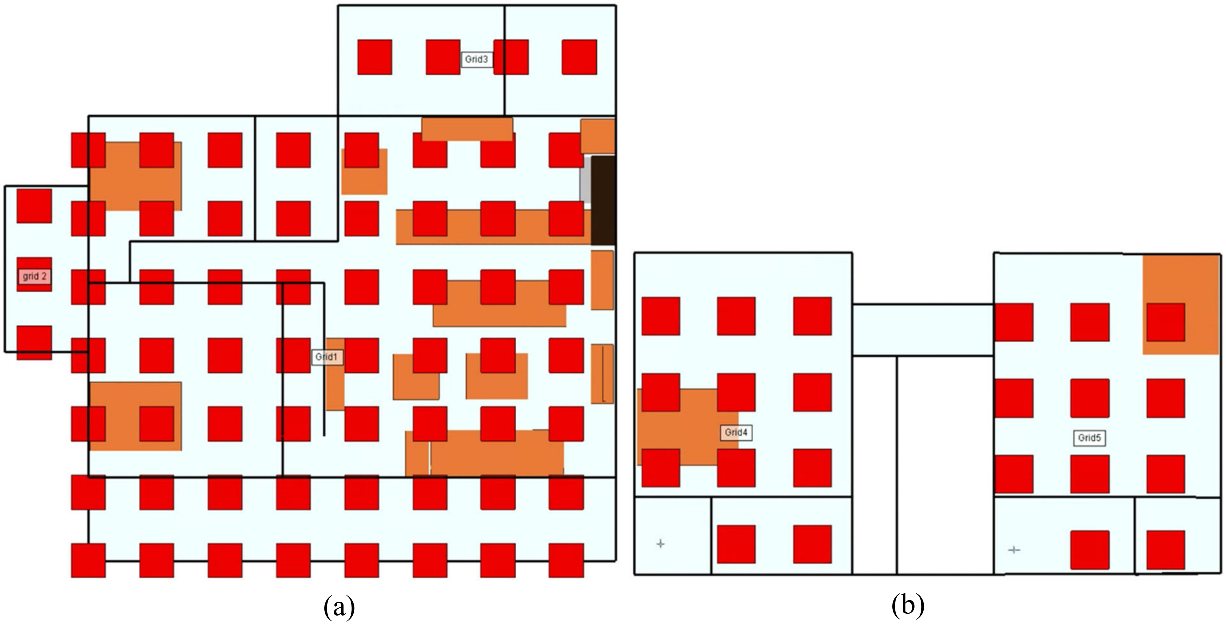

Fig. 4.12. Receiver locations in simulation model on (a) the bottom floor and (b) the top floor of a residential home.

Genetic algorithm (GA) optimization is used to determine the optimal transmitter position based on received power value by all the receivers. The cost function minimizes the number of receivers with received power lower than -87.5 dBm. Since one simulation takes over 15 minutes, parallel optimization is used to perform three simulations (limited by number of licenses) at one time, thereby reducing the time required to complete optimization. With additional Wireless Insite licenses, the time taken to achieve a desirable result will be further reduced.

.

The resulting transmitter position, chosen by the GA is shown in Figure 4.13. Received power values are only below -87.5 dBm in six receiver locations, shown in Fig. 4.14, which are mostly located in corners.

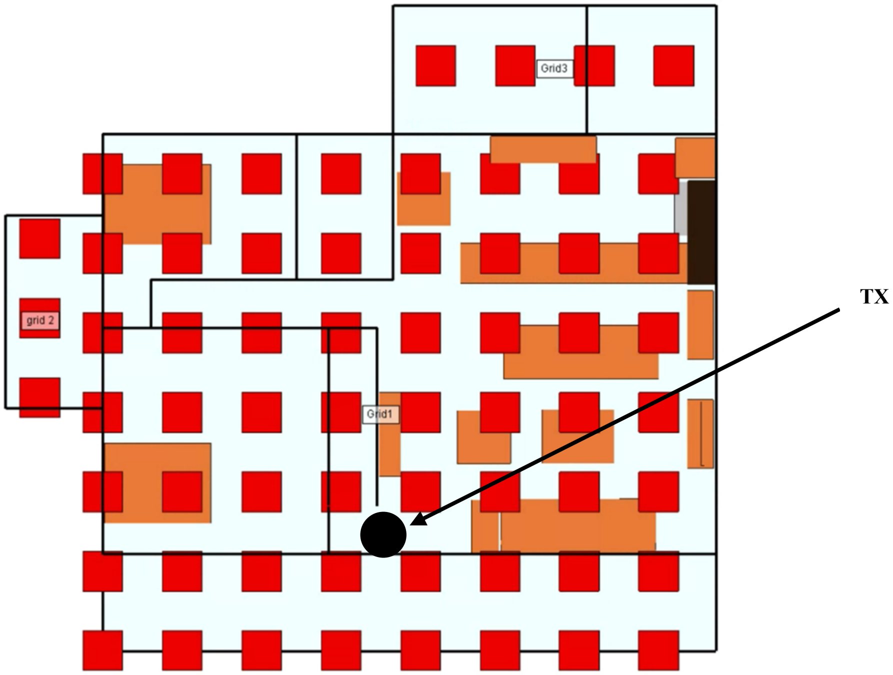

Figure 4.13. Optimal transmitter position for best coverage.

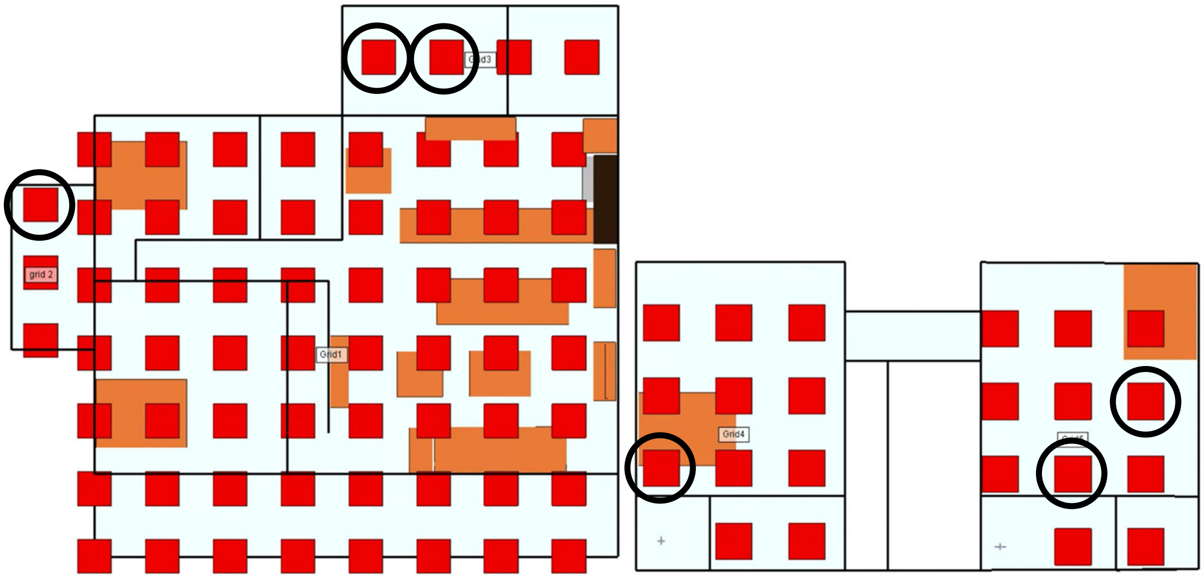

Figure 4.14. Receiver positions with less than -87.5 dBm received power on (a) the bottom floor and (b) the top floor of a residential home.

.

4.4 Summary

Wireless propagation is important to consider when designing a wireless communication system. In this work, various environments and applications of wireless propagation and ray tracing are studied. First, the Friis transmission equation is studied in the free-space environment and compared with behavior over dry earth and wet earth. It is observed that over dry and wet earth, received power decays more rapidly with distance, as opposed to in free space. It is also demonstrated that an increase in gain results in a proportional increase in received power values and a larger transmission distance.

The Georgia Southern University campus is investigated for full cellular coverage. Two repeater positions displayed desirable results, one with 19 receiver points below -87.5 dBm and the other with 180 receiver points below -60 dBm. In future work another repeater should be implemented to attain 100% coverage.

Lastly, genetic algorithm is used with parallel optimization to determine the optimal transmitter position in, a specific residential home. The parallel optimization technique allows for three instances with different receiver positions to be simulated at one time limited by the number of licenses available. The GA chosen position results in received power above -87.5 dBm at all but six receiver locations. In future work, additional transmitter locations may be used to improve for full coverage.

.

CHAPTER 5

FURTHER ANALYSIS IN A SIZE-REDUCED, 15-ELEMENT PLANAR YAGI ANTENNA[1]

5.1 Abstract

A size-reduced, 15-element, planar Yagi antenna is presented with comparable performance to the full-sized Yagi antenna. In recent works, many attempts have been made to design size-reduced Yagi antennas, however the full-sized Yagi antenna has the highest realized gain to date. By using rounded, T-shaped top loadings, an element-length reduction ratio of 45% compared to the full-sized Yagi is achievable, while maintaining bandwidth, efficiency, bandwidth-efficiency product ($B\eta$) and realized gain. The final antenna design is supported by a detailed design procedure, including a parametric study regarding the top-loaded dipole. Top-loaded dipoles of varying number of elements are compared with the full-sized counterparts to demonstrate T-shaped, top-loading effects on the Yagi antenna elements. The current distributions of the full-sized, 15-element Yagi and the size-reduced, 15-element Yagi antenna are studied to explain minor difference in realized gain. An extensive literature search is performed on size-reduced Yagi antennas, and gain enhanced LPDA antennas, emphasizing the novelty of the presented size-reduced Yagi Antenna.

5.2 Design Procedure

In [31], the importance of the top loading structure is demonstrated, through the GA optimization, for maximum omnidirectional directivity in the azimuth plane, of an arbitrarily wound wire antenna in a hemisphere with an electrical size, *kr*, of 0.88, as shown in Fig. 5.1(a). The top-loading structure and vertical antenna body are notable features of the geometry chosen by the GA. The top-loading structure facilitates resonance within a restricted volume. The strongest current is found on the vertical body, extending to the top of the hemisphere that encloses the antenna. This allows for the maximum directivity in the azimuth plane. Two-arm, spherical top-loading, shown in Fig. 5.1(b) is used to further decrease *kr* to 0.2, in [31].

---

[1] L. P. Smith, J. C. Howell and S. Lim, "A Size-Reduced, 15-Element, Planar Yagi Antenna," *IEEE Transactions on Antennas and Propagation*, doi: 10.1109/TAP.2020.3019564.

.

This further reduction in *kr* requires a much longer top-loading wire length to maintain resonance and an inductively coupled feed to step up the low-input resistance for impedance matching with the characteristic impedance of 50 Ω. The directivity pattern maintains the omnidirectionality with the maximum directivity in the azimuth plane, however bandwidth efficiency product, $B\eta$, is small. Implementation of a four-arm, spherical top-loading structure, with similar electrical size shows negligible performance differences. Therefore, a rounded, T-shaped, top-loaded, planar dipole geometry (Fig. 5.1(c)) is chosen to reduce the length of each individual element of the 15-element Yagi antenna, as demonstrated in Fig. 5.1(d). Previously, successful implementation of the T-shaped, top-loaded dipoles is demonstrated in [52],[53].

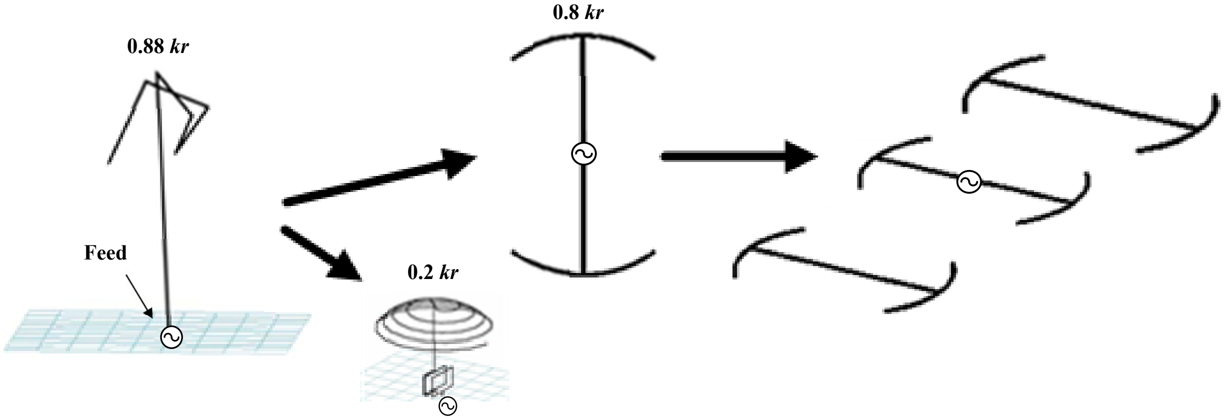

Fig. 5.1. Design methodology for the proposed size-reduced, planar Yagi antenna. © 2020 IEEE

Based on the Wheeler-Chu Limit presented in [54], as the antenna's electrical size decreases, the antenna has an increased difficulty maintaining the bandwidth-efficiency product ($B\eta$), which is the product of the fractional bandwidth and radiation efficiency. The equation for the theoretical $B\eta$ limit is

$$B\eta = \frac{1}{\sqrt{2}}\left(\frac{1}{kr} + \frac{1}{n(kr)^3}\right)^{-1}, \tag{4.2}$$

where B is the is the -10-dB impedance bandwidth, η is radiation efficiency, and *n* can either be 1 or 2: 1 is for linear or single-mode antennas, whereas 2 is for circular or dual-mode antennas. A value of 1 is chosen for *n*, since the antennas are linearly polarized. It is observed that the traditional full-sized dipole falls far below the theoretical limit of $B\eta$ (Fig. 5.2).

To determine the minimum electrical size, *kr*, that has a $B\eta$ closest to the theoretical limit and has similar $B\eta$ to that of the full-sized dipole, the T-shaped, top-loaded dipole antenna geometry is studied. The

.

reference antenna is a full-sized dipole designed with the minimum S_{11} at 1.5 GHz. The antenna has an electrical size of 1.45 *kr* after tuning and is constructed using copper wire with a diameter of 1.0 mm. Various T-shaped, top-loaded dipoles are then designed, varying in electrical sizes between 1.2 and 0.6, in decrements of 0.2. The different electrical sizes are attained by altering the vertical segment's length, which serves as the diameter of the sphere that encloses the antenna. Since each antenna is designed at the same resonant frequency, 1.5 GHz, the vertical segment's length is calculated by dividing the desired electrical size, by the constant wave number, *k*, and multiplying by two. Symmetrical top loadings are then added, with arc lengths determined by tuning for resonance with the minimum S_{11} at 1.5 GHz. The inset of Fig. 5.2 summarizes the geometries, dimensions and element-length reduction ratio compared with the full-sized dipole – which is calculated using the ratio of the electrical size of the top-loaded dipole to the electrical size of the full-sized dipole.

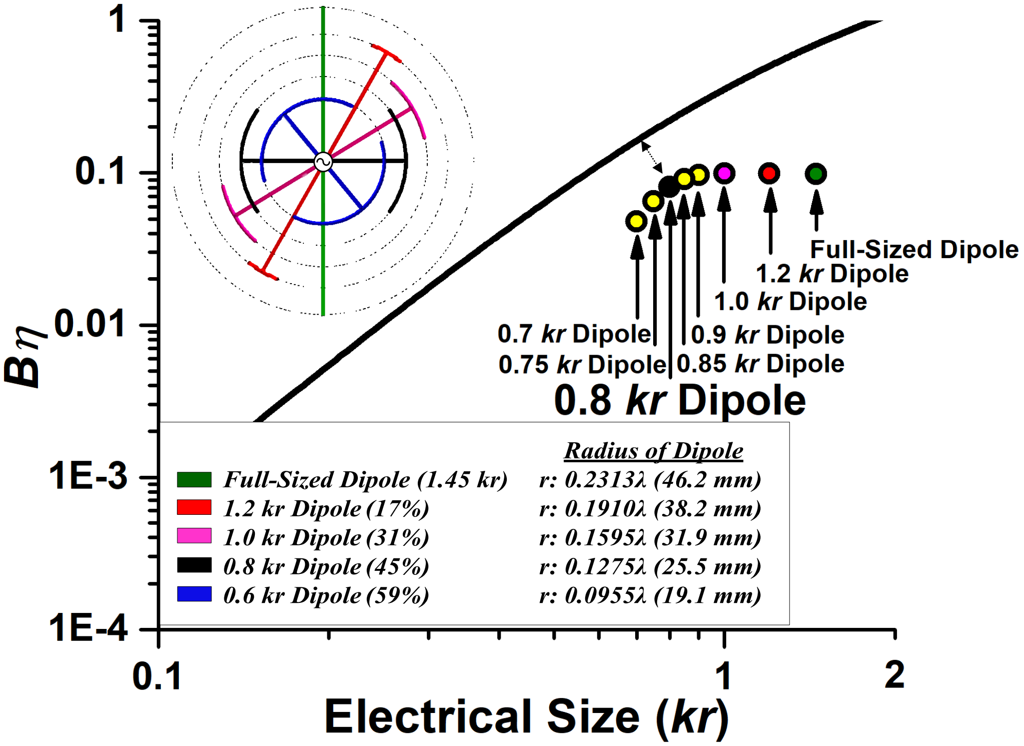

Fig. 5.2. Theoretical limit of bandwidth (*B*) - efficiency (*η*) product. © 2020 IEEE

Detailed simulation results and antenna parameters are recorded in Table V, including *kr*, element-length reduction ratio, -10-dB impedance bandwidth, radiation efficiency and *Bη*. The -10-dB bandwidth remains the same as the electrical size, *kr*, is gradually decreased for 1.45 to 1.0. Minor difference in bandwidth

.

is demonstrated in the 0.8 *kr* dipole in comparison to the full-sized dipole. The 0.6 *kr* dipole does not achieve -10-dB resonance due to the very small input resistance of 16.2 Ω at 1.5 GHz, while the input reactance is 0 Ω. The antenna is therefore poorly matched to the characteristic impedance of 50 Ω. Additional impedance matching techniques such as inductively coupled feed, multiple folding, or stub matching are avoided because, although they can be used to increase input resistance in a small size, $B\eta$ drops significantly, as exhibited in [31]. When the electrical size is decreased down to 0.8 *kr*, the radiation efficiency only has a minor difference. As a result, the $B\eta$ is the same as the full-sized dipole for the 1.2 *kr* and 1.0 *kr* dipoles, and slightly smaller for the 0.8 *kr* dipole. Additional dipoles, with electrical size in closer proximity to 0.8 *kr* are investigated for a closer study. For the antenna sizes smaller than 0.8 *kr*, $B\eta$ drastically decreases. The $B\eta$ for each dipole in the study is plotted in Fig. 5.2. The 0.8 *kr* dipole has the closest $B\eta$ to the theoretical limit, thus the minimum electrical size of a top-loaded dipole with a similar $B\eta$ to the full-sized dipole (1.45 *kr*) is chosen as 0.8 *kr*, which equates to a 45% element-length reduction ratio.

TABLE V © 2020 IEEE
T-SHAPED, TOP-LOADED DIPOLES COMPARISON

Electrical Size (*kr*)	Element-Length Reduction Ratio	-10-dB Impedance Bandwidth (*B*)	Radiation Efficiency (η)	$B\eta$
Full-sized (1.45)	-	9.9%	99.5%	0.099
1.20	17%	9.9%	99.4%	0.099
1.00	31%	9.9%	99.3%	0.099
0.90	38%	9.8%	99.1%	0.097
0.85	41%	9.2%	99.1%	0.091
0.80	**45%**	**8.2%**	**99.1%**	**0.081**
0.75	48%	6.6%	98.9%	0.065
0.70	52%	2.3%	98.6%	0.048
0.60	59%	×	94.5%	×

Next, the top-loaded dipole geometry is implemented in various Yagi antennas and compared to the full-sized versions. A full-sized dipole and a size-reduced dipole (with electrical size, *kr*, of 0.8) having the minimum S_{11} at 1.5 GHz are included for reference and are shown in Fig. 5.3(a) and (b), respectively. Fig. 5.3(c) shows a full-sized, two-element Yagi antenna designed at 1.5 GHz. It consists of a driver and a director. Next, a sized-reduced, two-element Yagi is designed at 1.5 GHz, as shown in Fig. 5.3(d). This is done by scaling the driver and director elements' straight-wire lengths by a factor of 0.55, since it is determined that the 0.8 *kr* dipole is optimal for the proposed antenna design. Similarly, a full-sized, three-element Yagi is designed at 1.5 GHz and consists of a driver, director, and reflector, shown in Fig. 5.3(e). Fig. 5.3(f) depicts a size-reduced, three-element Yagi, similarly designed at 1.5 GHz as the size-reduced, three-element Yagi in Fig. 5.3(d).

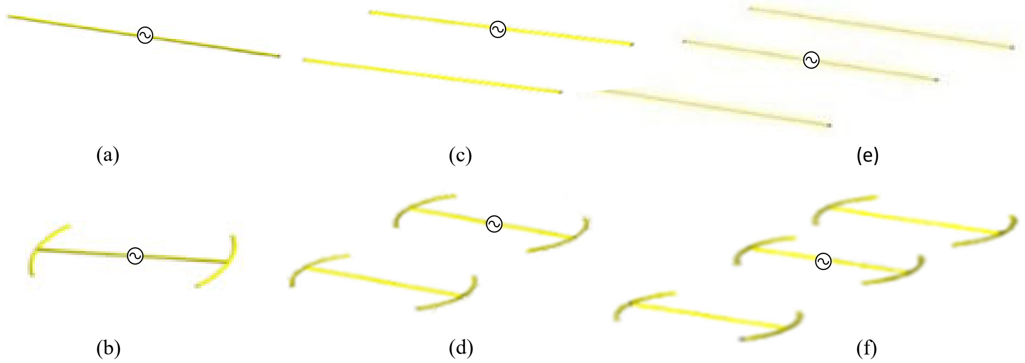
(a) (c) (e)

(b) (d) (f)

Fig. 5.3. Antenna geometries for the (a) full-sized dipole, (b) size-reduced dipole, (c) full-sized, two-element Yagi, (d) size-reduced, two-element Yagi, (e) full-sized, three-element Yagi, and (f) size-reduced, three-element Yagi antennas operating at 1.5 GHz. © 2020 IEEE

TABLE VI © 2020 IEEE

Size-Reduced Yagi Comparison with Different Number of Elements

Number of elements	Full-Sized / Size-Reduced	Area (cm^2)	-10-dB Impedance Bandwidth	Radiation Efficiency (η)	$B\eta$	Peak Realized Gain (dBi)
1	Full-Sized	-	9.9%	99.3%	0.099	2.0
	Size-Reduced	15.4	8.2%	99.1%	0.081	1.8
2	Full-Sized	55.6	8.0%	99.4%	0.080	3.9
	Size-Reduced	45.5	6.6%	99.5%	0.066	3.4
3	Full-Sized	87.1	6.5%	99.7%	0.065	8.3
	Size-Reduced	63.1	6.1%	99.8%	0.061	7.6

Table VI summarizes the simulation results for the Yagi antennas. As the number of elements increases, the size-reduced Yagi antenna's area reduction ratio compared to the full-sized Yagi antenna increases. The bandwidth difference between the size-reduced antenna and the full-sized one decreases as the number of elements increases. Radiation efficiency remains consistent as number of elements is changed, regardless of the antenna size, therefore, $B\eta$ differences are directly proportional to the bandwidth differences. In comparing the realized gains of the size-reduced antennas with the full-sized antennas, it is determined that the difference in their realized gains is approximately equal to a 0.2 dB contribution per each

.

additional element. The size-reduced dipole has a realized gain 0.2 dB less than the full-sized dipole. There is a 0.5 dB difference between the realized gains of the size-reduced, 2-element Yagi antenna and the full-sized, 2-element Yagi antenna. Finally, there is a 0.7-dB difference in realized gain between the size-reduced and full-sized Yagi antennas.

5.3 Current Distribution

The simulated current magnitude and phase are taken at the center of each element's vertical body in the full-sized Yagi and in the size-reduced Yagi and plotted in Fig. 5.4. The elements are labelled in numerical order from the front of the antenna to the back. The reflector is therefore element number 15. The antennas both have similar magnitudes on the first few elements, however the full-sized Yagi has higher current magnitude on the elements further away from the driver, which agrees with the difference in realized gain. The similar patterns of magnitude and phase demonstrate that the antennas are operating similarly.

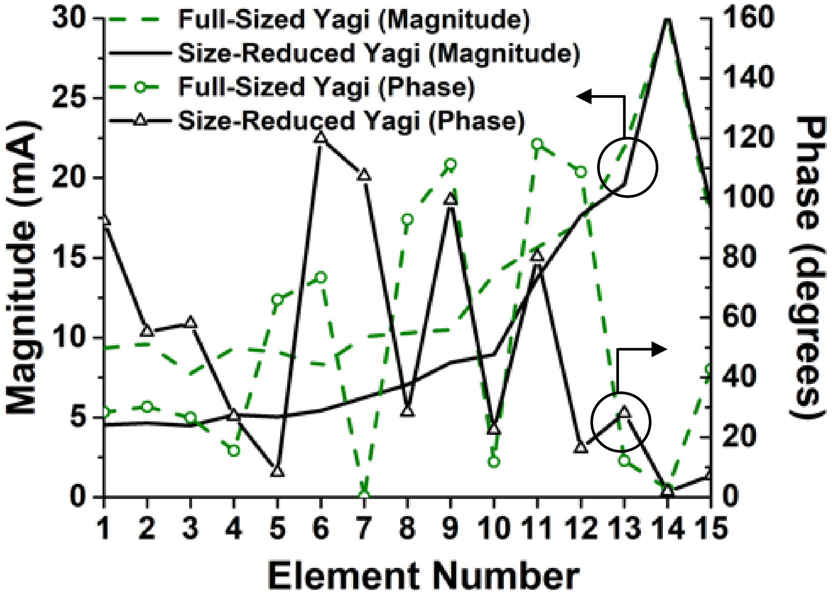

Fig. 5.4. Simulated current magnitude and phase distributions the size-reduced Yagi antenna. © 2020 IEEE

5.4 Antenna Comparison

An extensive literature search is conducted to illustrate the novelty of the presented antenna design and is summarized in Table VII. Although a very old design, the full-sized Yagi antenna has the highest realized gain to date. The presented size-reduced, Yagi antenna has the closest realized gain to the full-

.

sized one, while its element length is reduced by 45%. The antenna also maintains similar bandwidth, efficiency and $B\eta$ to the full-sized Yagi antenna.

TABLE VII © 2020 IEEE
COMPARISON OF SIZE-REDUCED YAGI ANTENNAS

	Planar or Printable Design	# of Elements	Impedance Bandwidth (B)	With / Without Ground Plane (GP)	Dipole / Monopole	Element-Length Reduction Ratio	Radiation Efficiency (η)	Peak Gain (dBi)	Peak Realized Gain (dBi)	Year
[13]*	No	3	1.9% (-3-dB)	Without GP	Dipole	0.0%	93.4%	7.1	7.1	2006
[13]*	No	3	1.3% (-3-dB)	With GP	Monopole	0.0%	-	-	9.9	2006
[14]	No	3	5.0% (-10-dB)	With GP	Monopole	0.0%	-	6.3	-	2011
[15]	No	3	10.2% (-3-dB)	With GP	Monopole	7.2%	>90%	-	9.5	2011
[16]	Yes	3	41.5% (-10-dB)	Without GP	Dipole	19.7%	-	6.0	-	2017
[17]	No	3	20.0% (-10-dB)	With GP	Monopole	16.6%	-	-	4.3	2010
[18]	No	3	6.5% (-10-dB)	Without GP	Dipole	19.4%	-	5.8	-	2011
[19]**	Yes	3	2.8% (-10-dB)	Without GP	Dipole	42.5%	-	6.3	-	2006
[19]***	No	3	1.4% (-10-dB)	Without GP	Dipole	43.2%	-	7.5	-	2006
[20]	Yes	3	10.5% (-10-dB)	Without GP	Dipole	11.7%	-	6.5	-	2016
[21]	No	3	1.2% and 0.2% (-10-dB)	With GP	Monopole	41.1%	98.1%	-	8.9	2014
[22]	No	5	21.6% (-10-dB)	With GP	Monopole	56.8%	-	7.2	-	2015
[23]	Yes	3	69.1% (-10-dB)	Without GP	Dipole	22.8%	-	4.5	-	2017
[24]	Yes	3	96.4% (-10-dB)	With GP	Dipole	0.0%	-	-	8.3	2014
[25]	Yes	2	3.7% (-10-dB)	With GP	Dipole	15.4%	98.6%	-	6.5	2015
[26]	Yes	15	3.3% (-10-dB)	Without GP	Dipole	47.4%	84.0%	11.5	-	2017
[27]	No	2	11.0% (-10-dB)	With GP	Dipole	35.2%	68.1%	5.5	-	2019
[28]	Yes	8	7.7% (-10-dB)	With GP	Dipole	14.4%	88.0%	10.6	-	2016
[29]	No	4	4.5% (-10-dB)	Without GP	Dipole	29.6%	-	-	4.6	2016
[30]	Yes	3	1.4% (-10-dB)	With GP	Dipole	13.1%	-	8.5	-	2017
Full-Sized Yagi	Yes	15	4.1% (-10-dB)	Without GP	Dipole	0.0%	99.4%	16.6	16.2	
Proposed Antenna	Yes	15	4.0% (-10-dB)	Without GP	Dipole	45.0%	99.5%	13.8	13.6	

All values are from simulation results since some antennas do not have measurement results.
*This publication contains both a monopole and dipole version.
**The planar design.
***The parallel design.

In [26], a split-ring resonator operating at the second resonant frequency is worth mentioning. The antenna has a 11.5-dBi gain with an element-length reduction ratio of 47.4%. However, with a similar element-length reduction ratio of 45%, the antenna presented in this work still exhibits 2.3 dB better gain (13.8 dBi), higher radiation efficiency of 99.5% (compared with 88%), and a slightly better bandwidth of 4.0% (compared with 3.3%). Table VIII also shows a comparison with recently published log-periodic dipole array (LPDA) antennas. Although there are high gain LPDA in recent works, since this is not the

.

main goal in its design, none of the antennas achieve as high a gain as the presented antenna, even with many more elements.

TABLE VIII © 2020 IEEE
COMPARISON OF PROPOSED YAGI ANTENNA WITH LPDA ANTENNAS

	# of Elements	-10-dB Impedance Bandwidth (B)	Element-Length Reduction Ratio	Radiation Efficiency (η)	Peak Gain (dBi)	Peak Realized Gain (dBi)
[52]	6	86.5%	48.5%	-	-	6.6
[55]	8	73.5%	33.2%	-	6.3	-
[56]	22	120.0%	41.1%	-	6.0	-
[57]	12	72.7%	26.3%	-	-	9.0
[58]	25	181.0%	8.8%	-	6.3	-
[59]	9	170.5%	22.8%	-	7.0	-
[60]	50	196.1%	25.1%	-	8.2	-
Proposed Antenna	15	4.0%	45.0%	99.5%	13.8	13.6

All values are simulated values. Element-length reduction ratio of LPDA antennas is calculated at the lowest frequency, since it is the dominating frequency in determining the electrical size of an antenna.

5.5 Summary

Further analysis of a size-reduced, planar 15-element antenna is performed to provide an in-depth explanation of the antenna's operation through introduction of the design procedure, parametric study about the rounded, T-shaped, top-loaded dipole geometry, and current distribution. A detailed literature search is conducted to highlight the novelty and importance of the presented antenna. Among all antennas compared, the presented antenna has the highest realized gain while its element-length is reduced 45% compared to the full-sized Yagi. The antenna also has similar performance in terms of bandwidth and efficiency.

.

CHAPTER 6

CONCLUSION

In this work, maximum power transmission is investigated in a variety of applications. First, radiative near-field wireless power transfer is studied. Many publications use various antenna geometries, at different operating frequencies, rectifiers and source powers so it is hard to compare the effectiveness of the antenna designs for the application. Commonly used antenna geometries are fairly compared, under similar conditions, in this work, and it is concluded that the meander antenna is ideal for radiative near-field wireless power transfer. Expansions of this work may include implementation of a phased array for Fresnel focusing and measurements for verification.

Next, a directive, UHF RFID tag is designed for pavement embedded purposes. The antenna can serve in a variety of applications including road work and possibly for smart cars. The presented antenna has size of $0.49\lambda \times 0.14\lambda \times 0.05\lambda$ and is well matched to the conjugate of the RFID chip impedance. Its bandwidth covers 72% of the US required bandwidth for UHF RFID, in measurement, and can be increased by implementing superposition of bowties with different flare angle and radii, on the driver element. The antenna has a directivity of 7.38 dBi in the direction of the director and a maximum reading range of 14.2 ft when it is placed just above the pavement. This is a significant improvement when compared to the 3.3 ft of the commercial tag. In future work, the behavior of the antenna when embedded into pavement should be taken into account.

Next, wireless propagation is studied in a variety of environments by using a ray-tracing software (Wireless Insite). The Friis Transmission Equation is studied in detail and it is demonstrated that the gain of an antenna is directly related to received power and transmission range. After the observation of lost cellular signal in specific areas on the Georgia Southern University campus, section of the campus is modelled for maximum cellular coverage. Two repeater positions are determined as ideal locations, with only 19 out of 729 receivers below -87.5 dBm and 180 out of 729 below -60 dBm, respectively. Additional repeaters may be implemented to further improve the coverage. A specific home is modeled and the best position for a 60 GHz router is determined by using parallel genetic algorithm optimization. The result is reasonable coverage, with only six receivers with received power less than -87.5 dBm. An additional transmitter may be used to improve results for full coverage.

Finally, a size-reduced, 15-element Yagi antenna is further investigated. The design procedure is described in detail, and a comprehensive literature search is provided to demonstrate the importance of the presented antenna. To date, no other size-reduced Yagi antenna attains such similar performance characteristics to the full-sized Yagi antenna as the presented antenna. The presented, size-reduced Yagi antenna has only 2.6 dBi difference in realized gain, and similar bandwidth and efficiency with an element-length reduction ratio of 45%.

.

REFERENCES

[1] S. S. Mohammed, K. Ramasamy and T. Shanmuganantham, "Wireless power transmission – a next generation power system," *Int. Jour. Comp. App.*, vol. 1, no. 13, 2010

[2] W.C. Brown, J.R. Mims, and NI. Heenan, "An experimental microwave-powered helicopter," *IEEE International Convention Record*, vol. 13, part 5, pp.225-235, 1965.

[3] Matsumoto, *et. Al.*, "MINIX project toward the solar power satellites --- rocket experiment of microwave energy transmission and associated plasma physics in the ionosphere," *ISAS space energy symposium,* pp 69-76, 1986.

[4] W. C. Brown, "The history of power transmission by radio raves," *IEEE Trans. Microw. Theory Tech.*, vol. 32, no. 9, pp. 1230-1242, 1984

[5] Lan Sun Luk, A. Celeste, P. Romanacce, *et. al.*, "Point-to-point wireless power transportation wireless power transportation in reunion island" *48th Int. Astron. Cong.,* pp. 6-10, 1997

[6] "Goodbye wires…". MIT News. 2007-06-07. http://web.mit.edu/newsoffice/2007/wireless-0607.html

[7] C. A. Balanis, *Antenna theory: analysis and design*, 3rd ed. New York: Wiley, 2005.

[8] B. J. DeLong, A. Kiourti and J. L. Volakis, "A radiating near-field patch rectenna for wireless power transfer to medical implants at 2.5 GHz," *IEEE Jour. Electromag., RF, Microw. Med. Bio.*, vol.2, no. 1, March 2018.

[9] A. Abidet al., "Wireless power transfer to millimeter-sized gastrointestinal electronics validated in a swine model," *Sci. Rep.*, Vol 7, 2017. Art. no. 46745.

[10] R. Das and H. Yoo, "A multiband antenna associating wireless monitoring and nonleaky wireless power transfer system for biomedical implants," *IEEE Trans. Microw. Theory Tech.*, vol. 65, no. 7, pp. 2485–2495, Jul.2017.

[11] A. Yeh, J. Ho, Y. Tanabe, E. Neofytou, R. Beygui, and A. Poon, "Wirelessly powering miniature implants for optogenetic stimulation," *Appl. Phys. Lett.*, vol. 103, no. 16, 2013, Art. no. 163701

[12] C. A. Balanis, *Antenna theory: analysis and design*, 2nd edition,

[13] S. Lim and H. Ling, "Design of a closely spaced, folded Yagi antenna," *IEEE Antennas Wireless Propag. Lett.,* vol. 5, pp. 302-305, 2006.

[14] Q. Xin et al., "Yagi-Uda antenna with small size for vehicles," *IET Elec. Lett.*, vol. 47, no. 7, pp. 428-430, 2011.

[15] D. Arceo and C. A. Balanis, "A compact Yagi-Uda antenna with enhanced bandwidth," *IEEE Antennas Wireless Propag. Lett.,* vol. 10, pp. 442-445, 2011.

.

[16] S. A. Rezaeieh, M. A. Antoniades, and A. M. Abbosh, "Miniaturized planar Yagi antenna utilizing capacitively coupled folded reflector," *IEEE Antennas Wireless Propag. Lett.,* vol. 16, pp. 1977-1980, 2017.

[17] G. C. Chen, K. K. Chan, and K. Rambabu, "Miniaturized Yagi class of antennas for GSM, WLAN and WiMax applications," *IEEE Trans. Cons. Elec.,* vol. 56, no. 3, pp. 1235-1240, 2010.

[18] J. A. Tirado-Mendez et al., "Inductively-loaded Yagi-Uda antenna with cylindrical cover for size reduction at VHF-UHF bands," *IEEE Trans. Antennas Propag.,* vol. 59, no. 2, pp. 357-362, Feb. 2011.

[19] Z. Bayraktar, P.L. Werner, and D.H. Werner, “The design of miniature three-element stochastic Yagi-Uda arrays using particle swarm optimization,” *IEEE Antennas Wireless Propag. Lett.,* vol. 5, pp. 22-26, 2006.

[20] Y. Luo, and Q. Chu, "A Yagi-Uda antenna with a stepped-width reflector shorter than the driven element," *IEEE Antennas Wireless Propag. Lett.,* vol. 15, pp. 564−567, 2016.

[21] J. Yu, Y. Le, and S. Lim, "Design of a dual-band, electrically small, parasitic array antenna," *IEEE Antennas Wireless Propag. Lett.,* vol. 13, pp. 1453−1456, 2014.

[22] Z. Hu, Z. Shen, W. Wu, and J. Lu, "Low-profile top-hat monopole Yagi antenna for end-fire radiation," *IEEE Trans. Antennas Propag.,* vol. 63, no. 7, pp. 2851-2857, Jul. 2015.

[23] S. Ahdi Rezaeieh, M. A. Antoniades, and A. M. Abbosh, "Miniaturization of planar Yagi antennas using mu-negative metamaterial-loaded reflector," *IEEE Trans. Antennas Propag.,* vol. 65, no. 12, pp. 6827-6837, Dec. 2017.

[24] J. Wu, Z. Zhao, Z. Nie, and Q. Liu, "Bandwidth enhancement of a planar printed quasi-Yagi antenna with size reduction," *IEEE Trans. Antennas Propag.,* vol. 62, no. 1, pp. 463-467, Jan. 2014.

[25] M. Tang, T. Shi, and R. W. Ziolkowski, "Flexible efficient quasi-Yagi printed uniplanar antenna," *IEEE Trans. Antennas Propag.,* vol. 63, no. 12, pp. 5343-5350, Dec. 2015.

[26] P. Aguilà, et al., "Planar Yagi–Uda antenna array based on split-ring resonators (SRRs)," IEEE Antennas Wireless Propag. Lett., vol. 16, pp. 1233-1236, 2017.

[27] I. Hwang, et al., "Quasi-Yagi antenna array with modified folded dipole driver for mmWave 5G cellular devices," *IEEE Antennas Wireless Propag. Lett.*, vol. 18, no. 5, pp. 971-975, May 2019.

[28] M. Farran, et al., "Compact quasi-Yagi antenna with folded dipole fed by tapered integrated balun," *Electron. Lett.,* vol. 52, no. 10, pp. 789-790, May 2016.

[29] R. Bhattacharya, R. Garg, and T. K. Bhattacharyya, "Design of a PIFA-driven compact Yagi-type pattern diversity antenna for handheld devices," *IEEE Antennas Wireless Propag. Lett.,* vol. 15, pp. 255-258, 2016.

[30] B. S. Abirami and E. F. Sundarsingh, "EBG-Backed flexible printed Yagi–Uda antenna for on-body communication," IEEE *Trans. Antennas and Propag.,* vol. 65, no. 7, pp. 3762-3765, Jul. 2017.

[31] S. Lim, "Analysis and design of electrically small antennas for non-line-of-sight communications," Ph.D. dissertation, The Univ. of Texas at Austin, Austin, 2007.

[32] P. Pérez-Nicoli, A. Rodríguez-Esteva and F. Silveira, "Bidirectional analysis and design of RFID using an additional resonant coil to enhance read range," *IEEE Trans. on Microw. Theory Techn.*, vol. 64, no. 7, pp. 2357-2367, Jul. 2016.

[33] I. Park and D. Kim, "Artificial magnetic conductor loaded long-range passive RFID tag antenna mountable on metallic objects," *IET Elect. Lett.*, vol. 50, no. 5, pp. 335-336, Feb. 2014.

[34] A. Goldsmith, *Wireless Communications*, Cambridge University Press, 2005.

[35] Z. Chen, H. Sun and W. Geyi, "Maximum wireless power transfer to the implantable device in the radiative near field," *IEEE Antennas and Wireless Prop. Lett.*, vol. 16, pp. 1780-1783, 2017.

[36] V. R. Gowda, et al, "Wireless power transfer in the radiative near field," in *IEEE Antennas and Wireless Prop. Lett.*, vol. 15, pp. 1865-1868, 2016.

[37] I. J. Yoon, and H. Ling, "Realizing Efficient Wireless Power Transfer in the Near-field region using electrically small antennas," *Wireless Power Transfer – Princ. and Eng. Expl.,* pp. 151-169.

[38] B. J. DeLong, A. Kiourti and J. L. Volakis, "A Radiating Near-Field Patch Rectenna for Wireless Power Transfer to Medical Implants at 2.4 GHz," *IEEE Jour. Electromag., RF and Microw. Med. Bio.*, vol. 2, no. 1, pp. 64-69, March 2018.

[39] J. Chen, Y. B. Le, and S. Lim, "A passive UHF RFID tag antenna for road marker navigation application," *2015 IEEE Internat. Symp. on Antennas Propag. USNC/URSI Nation. Radio Science Meeting*, Vancouver, Canada, Jul. 2015.

[40] H. Qin, Y. Peng and W. Zhang, "Vehicles on RFID: error-cognitive vehicle localization in GPS-less environments," *IEEE Trans. on Vehic. Tech.*, vol. 66, no. 11, pp. 9943-9957, Nov. 2017.

[41] S. Jeong and H. Son, "UHF RFID tag antenna for embedded use in a concrete floor," *IEEE Antennas Wireless Propag. Lett.*, vol. 10, pp. 1158-1161, 2011.

[42] R. J. Weiler, et al, "Environment induced shadowing of urban millimeter-wave access links," *IEEE Wireless Commun. Lett.*, vol. 5, no. 4, pp. 440-443, Aug. 2016.

[43] Y. J. Chun, et al, "A comprehensive analysis of 5G heterogeneous cellular systems operating over $\kappa - \mu$ Shadowed Fading Channels," *IEEE Trans. Wireless Comm.*, vol. 16, no. 11, pp. 6995-7010, Nov. 2017.

[44] J. Jung, J. Lee, J. Lee, Y. Kim and S. Kim, "Ray-tracing-aided modeling of user-shadowing effects in indoor wireless channels," *IEEE Trans. Antennas Prop.*, vol. 62, no. 6, pp. 3412-3416, June 2014.

[45] J. Holis and P. Pechac, "Elevation dependent shadowing model for mobile communications via high altitude platforms in built-up areas," *IEEE Trans. Antennas Prop.*, vol. 56, no. 4, pp. 1078-1084, April 2008.

[46] F. Yilmaz and M. Alouini, "A unified MGF-based capacity analysis of diversity combiners over generalized fading channels," *IEEE Trans. Comm.*, vol. 60, no. 3, pp. 862-875, March 2012.

.

[47] J. A. R. Azevedo and F. E. S. Santos, "An empirical propagation model for forest environments at tree trunk level," *IEEE Trans. Antennas Propag.*, vol. 59, no. 6, pp. 2357-2367, June 2011.

[48] Y. Li, M. Wu, A. E. Yilmaz and H. Ling, "Investigation of short-range radiowave propagation at HF/VHF frequencies in a forested environment," *IEEE Antennas Wireless Prop. Lett.*, vol. 8, pp. 1182-1185, 2009.

[49] D. L. Sachs and P. J. Wyatt, "A conducting slab model for electromagnetic propagation within a jungle medium," Radio Sci., vol. 3, pp. 125–134, 1968.

[50] D. Buhl and R. L. Rogers, "Experimental characterization of the forest as a medium for HF radio propagation," in *Proc. IEEE Antennas Propag. Soc. Int. Symp*., Jul. 2008, pp. 1–4.

[51] Y. S. Meng, Y. H. Lee, and B. C. Ng, "Empirical near ground path loss modeling in a forest at VHF and UHF bands," *IEEE Trans. Antennas Propag.*, vol. 57, no. 5, pp. 1461–1468, May 2009.

[52] J. Chen, J. Ludwig, and S. Lim, "Design of a compact log-periodic dipole array using T-top loaded dipoles," *IEEE Antennas Wireless Propag. Lett.*, vol. 16, pp. 1585–1588, 2017.

[53] M. Tang, R. W. Ziolkowski, S. Xiao, and M. Li, "A high-directivity, wideband, efficient, electrically small antenna system," *IEEE Trans. Antennas Propag*., vol. 62, no. 12, pp. 6541–6547, 2014.

[54] D. F. Sievenpiper *et al*., "Experimental validation of performance limits and design guidelines for small antennas," *IEEE Trans. Antennas Propag*., vol. 60, no. 1, pp. 8–19, Jan. 2012.

[55] G. Shin, *et al.*, "Gain characteristic maintained, miniaturized LPDA antenna using partially applied folded planar helix dipoles," *IEEE Access*, vol. 6, pp. 25874-25880, Jun. 2018.

[56] L. Chang, S. He, J. Q. Zhang, and D. Li, "A compact dielectric-loaded log- periodic dipole array (LPDA) antenna," *IEEE Antennas Wireless Propag. Lett.*, vol. 16, pp. 2759-2762, 2017.

[57] N. A. Bishop, *et a*l., "A broadband high-gain bi-layer LPDA for UHF conformal load-bearing antenna structures (CLASs) applications," *IEEE Trans. Antennas Propag.*, vol. 63, no. 5, pp. 2359-2364, 2015.

[58] K. Anim and Y. Jung, "Shortened log-periodic dipole antenna using printed dual-band dipole elements," *IEEE Trans. Antennas Propag.*, vol. 66., no. 12, pp. 6762-6771, Dec. 2018.

[59] G. Bozdag and A. Kustepeli, "Subsectional tapered fed printed LPDAantenna with a feeding point patch," *IEEE Antennas Wireless Prop. Lett.*, vol. 15, pp. 437-440, 2016.

[60] A. Kyei, D. Sim, and Y. Jung, "Compact log-periodic dipole array antenna with bandwidth-enhancement techniques for the low frequency band," *IET Microw. Antennas Propag.*, vol. 11, no. 5, pp. 711-717, Jan. 2017.